Numerical and Experimental Crack-tip Cohesive Zone Laws with Physics-Informed Neural Networks

H. Tran[1], Y.F. Gao[2], H.B. Chew[1,*]

1. Department of Aerospace Engineering, University of Illinois at Urbana-Champaign, Urbana, IL 61801, USA

2. Department of Materials Science and Engineering, The University of Tennessee, Knoxville, TN 37996, USA

*Author to whom all correspondence should be addressed. Email: hbchew@illinois.edu

Abstract The cohesive zone law represents the constitutive traction versus separation response along the crack-tip process zone of a material, which bridges the microscopic fracture process to the macroscopic failure behavior. Elucidating the exact functional form of the cohesive zone law is a challenging inverse problem since it can only be inferred indirectly from the far-field in experiments. Here, we construct the full functional form of the cohesive traction and separation relationship along the fracture process zone from far-field stresses and displacements using a physics-informed neural network (PINN), which is constrained to satisfy the Maxwell-Betti's reciprocal theorem with a reciprocity gap to account for the plastically deforming background material. Our numerical studies simulating crack growth under small-scale yielding, mode I loading, show that the PINN is robust in inversely extracting the cohesive traction and separation distributions across a wide range of simulated cohesive zone shapes, even for those with sharp transitions in the traction-separation relationships. Using the far-field elastic strain and residual elastic strain measurements associated with a fatigue crack for a ZK60 magnesium alloy specimen from synchrotron X-ray diffraction experiments, we reconstruct the cohesive traction-separation relationship and observe distinct regimes which suggest corresponding transitions in the micromechanical damage mechanisms.

Keywords: Cohesive zone law; crack growth; physics-informed neural networks; finite element method; synchrotron X-ray diffraction experiments

1. Introduction

The growth of cracks at locations of high stress concentrations, such as along adhesive joints, grain boundaries, and fiber-matrix interfaces, controls the macroscopic fracture and fatigue response of engineering materials (Chew et al., 2005; Li and Chew, 2016, 2017; Liu and Shin, 2019; VanSickle et al., 2020; Li et al., 2022; Jiang et al., 2023a). However, modeling the fracture and fatigue crack growth remains a challenge, since the complicated microscopic adhesive and cohesive damage processes at these high stress concentration sites are often inaccessible to direct experimental measurements. One well-established mechanistic approach to modeling crack growth or interface failure is to introduce an embedded fracture process zone (FPZ) ahead of the crack and to homogenize the localized deformation response within the FPZ into equivalent cohesive zone laws (Dugdale, 1960; Tvergaard and Hutchinson, 1992; Hutchinson and Evans, 2000; Guo et al., 1999; Gladysz and Chawla, 2020). These cohesive zone laws govern the relationship between the cohesive-zone tractions in equilibrium with the stress fields of the surrounding body and the cohesive-zone separations compatible with the deformation fields of the surrounding body (Akhavan-Safar et al., 2022), and can quantitatively represent detailed micromechanical failure processes, such as the nucleation, growth, and coalescence of voids (Allix and Corigliano, 1996; Guo et al., 1999; Cui et al., 2020; Muro-Barrios et al., 2022).

In the original Dugdale model (Dugdale, 1960), the cohesive traction is assumed to be a constant up until complete separation, but subsequent studies heuristically introduced different cohesive zone models, including the linear softening model (Hillerborg et al., 1976), a trapezoidal model (Tvergaard and Hutchinson, 1992), and an exponential model (Xu and Needleman, 1993; Gao and Bower, 2004; He and Xin, 2011). Nevertheless, studies often regard the cohesive strength (peak

traction) and the energy release rate (area under the traction-separation relation) as two primary material parameters governing crack advance and the macroscopic fracture behavior: the functional form of the cohesive zone law is assumed a priori, while these primary material parameters are calibrated with top-down experiments to best match the fracture resistance curves (Chen et al., 2003; Gustafson and Waas, 2009; Desai et al., 2016; Jemblie et al., 2017; Lélias et al., 2019). More recent studies show that the exact shape of the cohesive zone law represents the underlying crack growth micromechanics and is a key signature governing the fracture behavior of a material (Chandra et al., 2002; Kafkalidis and Thouless, 2002; Li and Chandra, 2003; Alfano, 2006; Olden et al., 2008; Alfano et al., 2009; Campilho et al., 2013; Chew, 2014; Heidari-Rarani and Ghasemi, 2017). For example, hydrogen embrittlement of stainless steel and high impact polystyrene (HIPS) are best represented by polynomial and concave-shaped cohesive zone laws, respectively, while crazing-induced ductile crack growth in polymethyl methacrylate (PMMA) resulted in a convex-shaped cohesive zone law (Hong et al., 2009). Even in the phase field fracture modeling where the crack path is not defined a priori, the equivalent cohesive zone law is found to have a shape similar to the governing hyperbole stiffness degradation function (Tran and Chew, 2022).

Elucidating the full functional form of the cohesive zone law, in addition to the cohesive parameters (e.g., peak traction, cohesive energy, complete failure separation), is a highly non-trivial inverse problem that is often subjected to ill-conditioning (Elices et al., 2002; Pierron and Lo, 2008). Cox and Marshall (1991) and Sørensen and Jacobsen (2003) heuristically determined the cohesive zone (or crack-bridging) laws in composite materials utilizing the crack opening displacement and the J-integral, respectively. Focusing on the crack-tip fields, Hong and Kim (2003) and follow-on studies (Chew et al., 2009; Hong et al., 2009; Kim et al., 2012) expressed the elastic fields of a crack tip with a cohesive zone in a homogeneous isotropic solid in terms of eigenfunction expansions in a complex mathematical form, where the inversion method is based on interaction J-integrals (Chen

and Shield, 1977). Chew extended this field projection (spectral) method by expressing the unknown tractions along an interface bounded by plastically-deforming materials in terms of the Fourier series, where the Fourier coefficients were determined using the Maxwell-Betti's reciprocal theorem with a reciprocity gap to account for nonlinear effects (Chew, 2013). Similar inversion methods utilizing series solutions were performed to quantify the continuum traction signatures along grain boundaries from atomistic stress information in the vicinity (Cui and Chew, 2022). The accuracy of such spectral methods requires that the assumed series solution accurately represents the functional form of the cohesive traction, and in turn, the cohesive separation, distributions. In the presence of non-periodic traction boundary conditions for an assumed periodic (e.g., Fourier) series solution, many terms in the series solution would then be needed to capture the sharp transitions or localized details in the traction or separation distributions. This significantly increases the sensitivity of the inverse solution to small numerical or experimental errors in the far-field measurement data (Chew, 2013; Willis, 1966).

Machine learning techniques based on deep neural network architectures have recently been applied to solving inverse problems in mechanics. For example, artificial neural networks (ANNs) trained on numerical datasets have successfully predicted the stress hotspots for cracking (Mangal and Holm, 2018, 2019; Pierson et al., 2019; Perera and Agrawal, 2023), the locations of dislocations from the atomistic stress fields of grain boundaries (Noh and Chew, 2024), the constitutive behavior of materials at both the atomistic and continuum scales (Rowe et al., 2020; Shaidu et al., 2021; Zhang et al., 2022; Li et al., 2023; Wang et al., 2023), as well as the stochastic crack growth in porous ductile materials (Worthington and Chew, 2023). In situations where there is sparse measurement data, a variant of deep ANNs, termed as physics-informed neural networks (PINNs), has the unique ability to solve both forward and inverse problems by constraining the solution to satisfy some predefined physical or governing laws (Cuomo et al., 2022; Rodriguez-Torrado et al., 2022; García-Cervera et

al., 2023; Seo, 2024). While originally formulated to solve partial differential equations in fluid problems, PINNs have recently been applied to the field of solid mechanics and interfacial failure modeling (Diao et al., 2023; Tao et al., 2023; Wei et al., 2023).

In this work, we inversely uncover the cohesive zone laws for fracture from far-field stress and displacement information using PINNs, which are constrained to satisfy Maxwell-Betti's reciprocal theorem. Section 2 details our PINN architecture applied to a small-scale yielding, mode I crack-growth problem in the finite element method (FEM). In Section 3, we study the generalizability of the PINN to reconstruct different functional forms of the cohesive zone laws in both linear elastic and elasto-plastic materials, using measurement data at varying domain sizes in the far-field. The PINN is subsequently used in Section 4 to reconstruct the cohesive traction-separation relationship for a ZK60 magnesium alloy from the elastic strain fields of a fatigue crack provided by synchrotron X-ray diffraction (S-XRD) experiments. Section 5 discusses the implications of our results in the context of prior inverse approaches and concludes with a summary.

2. Problem Formulation

2.1 Crack growth simulations

We first assess the ability of PINNs to reconstruct the crack-tip cohesive zone laws from the far-fields of a crack growth problem under mode I loading, by generating the crack-tip fields through a forward finite element simulation detailed in this subsection (Fig. 1). Our small-scale yielding, finite element model comprises of a semi-infinite centerline crack in a homogeneous, isotropic material with elastic modulus $E = 1$ GPa and Poisson's ratio $\nu = 0.3$ subjected to remote mode I (K_I) K-field loading under plane strain conditions (Fig. 1a). We consider both a linear elastic material, and an elasto-plastic material with the plastic response characterized by a J_2 flow theory which obeys a linear hardening relationship

$$\sigma_e = \sigma_y + \lambda \varepsilon^p \tag{1}$$

where σ_e is the von Mises stress, σ_y is the initial yield stress, ε^p is the plastic strain, and λ is the linear hardening constant. Along the remote circular boundary of the finite element mesh, we prescribe the elastic asymptotic K_I plane strain displacement fields

$$u_1(R,\theta) = K_I \frac{1+\nu}{E}\sqrt{\frac{R}{2\pi}}\,(3-4\nu-\cos\theta)\cos\frac{\theta}{2}$$
$$u_2(R,\theta) = K_I \frac{1+\nu}{E}\sqrt{\frac{R}{2\pi}}\,(3-4\nu-\cos\theta)\sin\frac{\theta}{2} \quad (2)$$

where $R = \sqrt{x_1^2 + x_2^2}$ and $\theta = \tan^{-1}\left(\frac{x_2}{x_1}\right)$ for points on the remote boundary (Fig. 1a). We conduct finite element simulations of the boundary value problem using the commercial finite element software, ABAQUS (Smith, 2009). The finite element mesh consists of 52,452 two-dimensional, plane strain 4-noded CPE4 linear elements (Fig. 1c).

To simulate crack propagation, we implement a single row of cohesive elements (Fig. 1b) located within a highly-refined mesh region ahead of the initial crack tip ($x_1 = x_2 = 0$) comprising of uniformly-sized elements, each of dimensions $D \times D$ (Fig. 1d). These cohesive elements obey a prescribed relationship between the normal cohesive traction t_2 and the normal cohesive separation δ_2, with t_0 denoting the peak traction, δ_0 the final separation (i.e., full damage), and Γ_0 the area under the traction-separation relation (Fig. 1b). Under the conditions of crack advance, the crack growth resistance Γ is related to the mode I stress intensity factor K_I by

$$\Gamma = \frac{1-\nu^2}{E} {K_I}^2 \quad (3)$$

In a linear elastic medium, $\Gamma_0 = \Gamma$. In an elasto-plastic medium, however, Γ has combined contributions from both the initial or intrinsic fracture energy associated with the process zone Γ_0, and the background plasticity Γ_p; small-scale yielding conditions prevail since the plastic zone size is small compared to the distance to the remote boundary R.

2.2 Neural network architecture

In physical experiments, the far-field strain or displacement information (∂R_2 in Fig. 1d) can be obtained with high accuracy using well-established techniques such as high-resolution digital image correlation (DIC) or neutron diffraction. However, direct, quantitative measurements within the narrow process zone ahead of the crack (∂R_1 in Fig. 1d) are generally not possible since this is the regime where the complicated micromechanics of fracture occur. Here, we seek to extract the unknown traction $t_2(x_1)$ and separation $\delta_2(x_1)$ distributions for material points located along ∂R_1 ($x_2 = 0$), from the measured stress $\sigma_{ij}(x_1, x_2)$ and displacement information $u_j(x_1, x_2)$ along ∂R_2. The traction (t_2) versus separation (δ_2) relationship is then obtained by combining the response of all material points along the crack face (∂R_1).

Fig. 2a depicts the architecture of our PINN, which takes an $[N \times 1]$ spatial matrix, $\mathbf{X_1}$, representing the x_1 coordinates of N collocation (material) points along ∂R_1, as an input. This input matrix is linearly connected to an ANN, comprising of several hidden layers, each with a fixed number of nodes per layer. The nodes within each hidden layer apply a series of weighting functions and biases to the previous layer before passing them onto the next layer through an activation function (Da Silva et al., 2017). The final hidden layer of the network linearly outputs two $[N \times 1]$ spatial matrices $\mathbf{T_2}$ and $\mathbf{D_{2,1}}$, representing the cohesive traction t_2 and separation gradient $\delta_{2,1} = \frac{\partial \delta_2}{\partial x_1}$, respectively, corresponding to each collocation point in $\mathbf{X_1}$. We cumulatively integrate $\delta_{2,1}$ in $\mathbf{D_{2,1}}$ using the composite trapezoidal rule to obtain δ_2 (and the spatial matrix $\mathbf{D_2}$), while enforcing the separation δ_2 to be the same at the common node between ∂R_1 and ∂R_2 at the end of the cohesive zone (node b in Fig. 1d).

We introduce three separate loss functions (L_1, L_2, L_3) in our PINN. The first function constrains the output cohesive tractions $\mathbf{T_2}$ to follow the known boundary tractions t_2 at the common nodes between ∂R_1 and ∂R_2 (nodes a and b in Fig. 1d)

$$L_1 = \big(t_2(a) - \mathbf{T_2}(a)\big)^2 + \big(t_2(b) - \mathbf{T_2}(b)\big)^2 \tag{4}$$

The second loss function enforces $\delta_2 \geq 0$ and $\delta_{2,1} \leq 0$ along ∂R_1 to ensure positive separation which continuously decays with distance from the crack-tip

$$L_2 = \frac{1}{N}\sum_{i=1}^{N}\left\{(\mathbf{D_2}(i) - |\mathbf{D_2}(i)|)^2 + \left(\mathbf{D_{2,1}}(i) + \left|\,\mathbf{D_{2,1}}(i)\right|\right)^2\right\} \tag{5}$$

The third loss function is the main driving loss which constraints the output traction and separation distributions to satisfy the Maxwell-Betti's reciprocal theorem. In a linear elastic problem, the Maxwell-Betti's reciprocal theorem relates the unknown tractions (t_2) and displacements ($u_2 = \delta_2/2$) along ∂R_1 to the measured tractions ($t_j = \sigma_{ij}n_i$) and displacements (u_j) along ∂R_2, i.e.,

$$\int_{\partial R_1} \hat{t}_2 u_2 - t_2 \hat{u}_2 dx_1 = \int_{\partial R_2} \hat{\sigma}_{ij} n_i u_j - \sigma_{ij} n_i \hat{u}_j dS = \mathcal{M} \tag{6}$$

where n_i is the outward normal to the boundary, $\mathcal{M}$ denoting the value of the integral based on measurement data along ∂R_2, and $S[\sigma_{ij}, u_j]$ and $\hat{S}[\hat{\sigma}_{ij}, \hat{u}_j]$ denote the real and auxiliary deformation fields of the same linear elastic material (Fig. 2b). Thus, the unknown solutions for $\mathbf{T_2}(i)$ and $\mathbf{D_2}(i)$ along ∂R_1 should satisfy (6) for all admissible auxiliary fields $\hat{S}[\hat{\sigma}_{ij}, \hat{u}_j]$. Augmentations to (6) through a reciprocity gap to account for (nonlinear) elasto-plastic effects are detailed later in Section 3.2. We select two classes of analytical auxiliary fields $\hat{S}_1$ and $\hat{S}_2$, depicted in Fig. 2b, representing the elastic half-space solutions for (i) an imposed periodic sin or cos distribution of normal $\hat{t}_2$ surface tractions, and (ii) a traction-free surface ($\hat{t}_1 = \hat{t}_2 = 0$) but with non-zero periodic sin or cos distributions of $\hat{u}_1$ and $\hat{u}_2$ displacement combinations, as detailed in Appendix A. With these two classes of auxiliary fields subjected to sin or cos distributions of tractions or displacements, each loading wavenumber k therefore provides 4 independent auxiliary fields. Considering k to range from 1 to n, we would have a total of $4n$ independent auxiliary fields, which we denote by the superscript m in $\hat{S}^m[\hat{\sigma}_{ij}^m, \hat{u}_j^m]$. Thus, the third loss function can be expressed as

$$L_3 = \frac{1}{4n}\sum_{m=1}^{4n}\left\{\int_a^b \left(\frac{1}{2}\hat{t}_2^m \mathbf{D_2} - \hat{u}_2^m \mathbf{T_2}\right) dx_1 - \mathcal{M}^m\right\} \tag{7}$$

where the integral is evaluated along ∂R_1 using the trapezoidal rule. We consider the relative contribution (w_i) of each loss component (L_i), to obtain the total loss

$$L_s = w_1 L_1 + w_2 L_2 + w_3 L_3 \tag{8}$$

The total loss in (8) is then backward propagated through the network to update the weights and biases of the ANN. The ratios of $w_1 : w_2 : w_3$, along with the number of wavenumbers (n), and hence the total number of auxiliary fields (= $4n$), are considered as hyperparameters of our PINN.

2.3 Hyperparameter study

We perform hyperparameter testing of the network structure by systematically varying the number of hidden layers, the number of nodes within each hidden layer, the learning rate, the type of activation function, and the relative weight contribution in the loss function. We evaluate the performance of each PINN architecture based on its ability to minimize the loss function L_s. At the epoch corresponding to this minimum L_s, we also separately calculate the root mean squared errors (RMSE) between the PINN-predicted traction-separation relationship versus the actual cohesive zone law implemented in FEM. Our simulations for the hyperparameter studies are based on an exponential cohesive zone model that is implemented in Abaqus as a UEL User Element subroutine (Gao, 2016)

$$\frac{t_2}{t_0} = \frac{\delta_2}{\delta_0} \exp\left(1 - \frac{\delta_2}{\delta_0}\right) \tag{9}$$

with a peak traction of $\frac{t_0}{E} = 0.003$, total separation of $\frac{\delta_0}{D} = 0.125$, and an intrinsic fracture energy of $\frac{\Gamma_0}{ED} = 0.000375$. Our FEM crack growth model is loaded to a sufficiently large K_I to enable crack propagation to a distance of $\Delta a = 80D = 640\delta_0$ from the initial crack-tip. Displacement and stress data are then taken along a predefined ∂R_2 located at a vertical distance of $h = 20D$ from the cohesive interface along ∂R_1 (Fig. 1d) at this crack instant for the reconstruction of the cohesive zone laws, though the effects of h/D are later studied in Fig. 6.

In the hyperparameter studies in Table 1, we choose the maximum wavenumber of $n = 7$ which provides us with a total of $4n = 28$ unique auxiliary fields. To increase the convergence rate, reduce the number of computations, and avoid the solution from getting trapped at the non-optimal local minima, we employ a Stochastic Gradient Descent approach (Shalev-Shwartz and Ben-David, 2014) where for each epoch, we randomly select only a proportion $p = 0.214$ (6 out of 28) of these auxiliary fields to compute the loss function L_s. The loss is then backward propagated through the network to update the weights and biases of the neural network before moving to the next epoch, where the process is repeated with a new $4np$ number of auxiliary fields selected at random out of the total $4n$ unique auxiliary fields. Note that if $p = 1$, we recover the traditional Gradient Descent (Shalev-Shwartz and Ben-David, 2014). We conduct this training process over 500,000 epochs using the Adam Optimizer (Da Silva et al., 2017).

Our results in Table 1 show that the number of hidden layers, together with the number of nodes per hidden layer, in the neural network are the most critical hyperparameters. Fig. 3a compares the (exponential) traction-separation law implemented in FEM (symbols) with the predictions of the PINN for varying number of layers and nodes per layers (lines). A PINN architecture with more layers than nodes per layer (purple line) completely fails to capture traction-separation relationship and tends to have extremely high L_s as shown in Table 1. In contrast, PINN architectures with fewer layers tend to capture the peak traction, final separation, and in general, the full functional form of the cohesive zone law, with high precision (red/blue/black lines in Fig. 3a). We select an optimal network structure comprising of 10 hidden layers with 30 nodes per layer (black line in Fig. 3a), which has the second lowest L_s, along with the lowest RMSE in the predicted traction-separation response. Our hyperparameter studies in Table 1 and Fig. 3b further show that the cohesive zone predictions are optimal with a learning rate of $l_r = 2 \times 10^{-5}$. Another important hyperparameter is the relative weight contributions in the loss function. Setting $w_3 \geq 10^4$ relative to $w_1 = w_2 = 1$ is

necessary to maintain low L_s and RSME values (Table 1, Fig. 3c), implying that satisfying the Maxwell-Betti's reciprocal theorem (L_3 in (7)) is key to ensuring accurate traction-separation predictions. Nevertheless, maintaining the boundary tractions (L_1 in (4)) is important, as shown by the significant errors introduced by setting $w_1 = 0$ (purple line, Fig. 3c). In comparison, enforcing the L_2 constraint in (5) to ensure positive and continuously decaying separations only marginally improves L_s (compare results for $w_2 = 0$ and $w_2 = 1$ with identical w_1, w_3 values under *Weight Contribution* in Table 1). Based on these studies, we enforce all three loss constraints, and with a relative weight contribution of $w_1 : w_2 : w_3 = 1 : 1 : 10^4$. Finally, while the choice of ELU, ReLU, and tanh activation functions does not significantly influence L_s and the associated RMSE values (Table 1), it affects the smoothness of the predicted traction-separation response (Fig. 3d) which can be important for numerical stability when these cohesive zone law predictions are implemented in FEM. As such, we select the ELU activation function for our final PINN architecture. Note that our PINN-extracted cohesive zone laws in Fig. 3 do not start precisely at $t_2 = \delta_2 = 0$, since $t_2(x_2) = 0$ lies beyond the extraction region of ∂R_1 in Fig. 1d.

The demonstrated importance of the Maxwell-Betti's reciprocal theorem governing L_3 in (7) introduces two additional hyperparameters that can influence our network performance: (a) the number of unique auxiliary fields ($4n$), and (b) the proportion p of these $4n$ terms enforced at each epoch in the L_3 constraint. Fig. 4 examines the effects of Stochastic Gradient Descent by comparing the loss evolution and the predicted traction-separation laws with increasing epochs for varying p with a fixed $n = 7$. The use of Stochastic Gradient Descent with $p = 0.214$ in Fig. 4a results in noisy L_s with traction-separation response converging only after epoch (iii). In contrast, the traditional Gradient Descent approach ($p = 1$) in Fig. 4b is characterized by very smooth loss evolution leading to rapid convergence after epoch (ii) in the predicted traction-separation response. One of the distinct advantages of Stochastic Gradient Descent is its computational efficiency, since only a smaller subset

of $4np$ (out of $4n$) functions are evaluated at each epoch. Interestingly, the predicted traction-separation response with $p = 0.214$ is noticeably closer to the implemented exponential response in FEM, highlighting the Stochastic Gradient Descent's ability to converge towards the global minimum, while the solution for the traditional Gradient Descent ($p = 1$) can be trapped at a local minimum. Further reduction in the number of evaluated functions per epoch to just a single function ($4np = 1$) with $p = 0.036$ in Fig. 4c significantly increases fluctuations in L_s. We now arrive at a converged solution at a higher epoch ((iv) and beyond), but with observable differences between the predicted and actual cohesive zone laws.

Conceivably, a larger n will result in better agreement between the reconstructed cohesive traction and separation distributions from PINN versus the ground truth data from FEM, since more physical constraints are enforced to nudge the solution towards satisfying (7). In reality, our results for the converged traction-separation predictions across various combinations of p and n values in Fig. 5b-d show no discernable improvement in the PINN predictions beyond $n \geq 3$, regardless of the number of enforcing functions, $4np$. In fact, even with $4np = 1$ in Fig. 5a, where the reciprocal theorem is enforced for a single auxiliary field per epoch, we still obtain reasonable predictions with $n = 5$ and beyond. Close examination shows that the pre- and the post-peak of the cohesive zone law are marginally better captured with $n = 3, 4np = 6$ (purple in Fig. 5c,d) and $n = 9, 4np = 6$ (blue in Fig. 5d), respectively.

3. Numerical Reconstruction of Crack-tip Cohesive Zone Laws

3.1 Generalization capabilities

We have demonstrated the ability of our PINN to numerically reconstruct an exponential cohesive zone law along the crack face (∂R_1) from field displacement/stress information at a vertical distance $h(= 20D)$ away (along ∂R_2). For the PINN approach to be useful, it must be capable of performing the reconstruction based on available data at different domain heights from the crack interface. It

should also be generalizable to different functional forms of the cohesive zone law which are typically unknown a-priori in experiments. As in classical inverse problems, using information from the far field ∂R_2 generally leads to ill-conditioning, where the extracted results could be highly sensitive to numerical (interpolation) errors and uncertainties in the input measurements (Elices et al., 2002; Pierron and Lo, 2008). The effects of ill-conditioning are exacerbated with increasing distance h of the measurement data from the domain of interest (crack face).

Fig. 6 depicts the PINN predicted exponential traction-separation relationship for three sets of n and p combinations based on measurement data along different h/D. Note that $h = 80D$ constitutes the exterior of the highly-refined mesh surrounding the propagating crack (green box in Fig. 1d), and we use the interpolated stress and displacement information for the non-structured 4-node elements along ∂R_2 in our computations of (6) to (8) for $h > 80D$. Results show that the PINN predictions of the cohesive tractions and separations are very accurate for $h \leq 40D$ $(= 320\ \delta_0)$, and follows closely to the ground truth cohesive zone law implemented in FEM (symbols). Accuracy of the predictions are slightly reduced with larger domain sizes, but the general functional form of the traction-separation relationship is still correctly captured with very accurate t_0, δ_0, and Γ_0 predictions even at $h = 140D$ $(= 1120\ \delta_0)$, where the maximum normal stress σ_{22} along ∂R_2 has dropped by 60% compared to the peak cohesive traction t_0. Beyond this domain at $h = 160D$ $(= 1280\delta_0)$, however, our PINNs for $n = 3$ and $n = 9$ in Figs. 6a and 6b fail to capture the cohesive zone relation, though the notably better predictions with $n = 2, p = 1$ in Fig. 6c suggests that this issue can be somewhat mitigated by limiting the enforcement of L_3 to lower-order auxiliary fields.

Our cohesive zone reconstructions thus far are based on an exponential traction-separation relation in (9). Next, we elucidate the ability of our PINN to reconstruct a variety of cohesive zone shapes (symbols in Fig. 7) widely adopted in the literature (Dugdale, 1960; Hillerborg et al., 1976; Tvergaard and Hutchinson, 1992; Xu and Needleman, 1993; Chen et al., 2003; Li and Chandra, 2003;

Alfano, 2006; Hong et al., 2009; Heidari-Rarani and Ghasemi, 2017; Tran and Chew, 2022; Akhavan-Safar et al., 2022): convex (a,b), concave (c,d), Dugdale (e), trapezoidal (f,g), polynomial (h,i), and bilinear (j,k,l). We implement each of these cohesive zone laws using a User Element Subroutine, and propagate each crack to a crack distance of at least $\Delta a = 20D$ or until the separation is fully developed at the crack wake. Using the numerically-obtained stress and displacements along a predefined ∂R_2 located at $h = 20D$ from the crack-face, we enforce (7) and (8) with the auxiliary fields for $n = 3$ and $n = 9$, using the same number of functions evaluated per epoch of $4np = 6$. We consider the solution of each PINN to converge when the minimum L_s remains unchanged for the next 200,000 epochs, and we include these converged PINN predictions (red and blue curves) in Fig. 7. For reference, we also include the predicted traction and separation distributions in Figs. S1 and S2 of the Supplementary Materials.

For cohesive zone laws with convex, concave, polynomial, or bilinear functional forms, our PINN predictions based on $n = 3$ and 9 are both in very good agreement with the actual cohesive zone laws (symbols), although the former is better able to capture the peak cohesive traction t_0. Interestingly, the PINN prediction based on $n = 9$ is able to replicate fairly well the Dugdale-shaped cohesive zone law, which is characterized by constant peak traction t_0 for long periods of separation. Both PINNs however overestimate the peak tractions for trapezoidal-shaped cohesive zone laws. Potentially, an optimal network architecture exists (e.g., different combinations of n, p or even different number of hidden layers and nodes per layer) that can better fit the functional forms of these cohesive zone relations individually. In practice, one has no information on the shape of the cohesive zone law a-priori. Nevertheless, we conclude based on our analyses in Fig. 7 that our PINN architecture (assuming $n = 3,9$ with $4np = 6$) accurately predicts the full functional form of the crack-tip cohesive zone law from far-field measurements.

3.2 Extensions to elasto-plastic medium

The Maxwell-Betti's reciprocal theorem is strictly applicable to linear elastic medium. For an elasto-plastic material characterized by $\sigma_y/E = 0.0012$ and $\lambda = 0.15$ in (1) with the same exponential cohesive zone law in (9), we plot the von Mises stress contours in Fig. 8a at the current loading of $K_I = K_{max}$ $(= 0.87ED)$ and after unloading from K_{max} to 0. We observe significant build-up of residual stress caused by plastic deformation during crack propagation after the crack is fully unloaded to $K_I = 0$. We select 8 material points (cross symbols) surrounding the current crack-tip and trace the history of the local equivalent stress (σ_e) versus equivalent strain (ε_e) at each of these material points in Fig. 8b as the crack is loaded from its undeformed reference state (filled circle symbol) to K_{max} (cross symbols). While all material points initially follow a stress-strain response defined by (1), material points 2, 3, 6, 7 behind the current crack wake are linearly unloaded once the crack propagates.

Neglecting plasticity effects, we first use the optimized PINN architecture from Section 2 and extract the equivalent cohesive zone law from measurement data about two distinct domains at $K_I = K_{max}$: ∂R_2^i and ∂R_2^{ii} located at $h = 20D$ and $80D$ above the crack face (solid and dash line in Fig. 8a-top, respectively). Fig. 9a compares the PINN-predicted traction distribution $t_2(x_2)$, separation distribution $\delta_2(x_2)$, and the traction-separation relationship (solid and dashed curves) versus the ground truth exponential cohesive zone law (symbols). Observe that the PINN prediction depends on the path (∂R_2^i or ∂R_2^{ii}) where the measurement data is taken, suggesting the loss of path-independence of the reciprocal theorem. While the corresponding PINN-predicted separation distributions are largely similar, an abrupt decrease in separation is observed beyond $x_1 > 150D$ due to the constraint enforcing δ_2 to be the same at the common node b between ∂R_1 and ∂R_2 in Fig. 1d when integrating $\mathbf{D_{2,1}}$ to obtain $\mathbf{D_2}$ in Fig. 2a. Together, the traction-separation predictions based on measurement data from the outer domain ∂R_2^{ii} envelopes the predictions based on the inner domain ∂R_2^i. The assumption of linear elasticity in the reciprocal theorem infers that the traction-separation predictions from each

domain can be interpreted as the equivalent cohesive zone law with a linear elastic material assumption within ∂R, where all plasticity effects within the projected domain ∂R are embodied within the extracted cohesive zone law. Therefore, the PINN predictions are similar to the actual cohesive zone law for smaller h/D. For larger h/D, the predicted cohesive energy (area under the traction-separation response) would be higher, since it encompasses both the intrinsic fracture energy within the process zone and the background plastic dissipation within ∂R. At sufficiently large h/D, where the entire background plasticity is encompassed within ∂R, the cohesive energy of the PINN-predicted cohesive zone law will equate with Γ in (3).

The stress σ_{ij} and displacement u_j fields at the current deformed configuration of $K_I = K_{max}$ are based on the undeformed state (filled circle symbol in Fig. 8b) as reference material configuration. Recently, Tran et al. showed that the deformation response of an elasto-plastic material (with linear unloading) at its current $K_I = K_{max}$ configuration can be reformulated as a linear elastic-equivalent material by considering the unloaded configuration to $K_I = 0$ from K_{max} as its new reference configuration (Tran et al., 2022). Accordingly, we treat this new unloaded crack at $K_I = 0$ as the new reference configuration; corresponding expressions for stress, strain, and displacements herein are denoted with a '~' accent in this new reference configuration. Based on the principle of superposition, the current strain relative to this new reference state, $\tilde{\varepsilon}_{ij}$, is related to the elastic strain, ε_{ij}^{el}, and the residual elastic strain after unloading to $K_I = 0$, ε_{ij}^{res}, by

$$\tilde{\varepsilon}_{ij} = \varepsilon_{ij}^{el} - \varepsilon_{ij}^{res} \tag{10}$$

where both ε_{ij}^{el} and ε_{ij}^{res} are relative to the original undeformed configuration. The current stress relative to this new reference state, $\tilde{\sigma}_{ij}$, can be expressed as

$$\tilde{\sigma}_{ij} = C_{ijkl}\tilde{\varepsilon}_{ij} = \sigma_{ij} - \sigma_{ij}^{res} \tag{11}$$

where C_{ijkl} is the elastic stiffness tensor, and $\sigma_{ij}^{res} = C_{ijkl}\varepsilon_{kl}^{res}$ is the residual stress after unloading to $K_I = 0$. To illustrate this, we apply (10) and (11) to the same 8 material points in Fig. 8a to compute

the equivalent von Mises stress ($\tilde{\sigma}_e$) versus strain ($\tilde{\varepsilon}_e$) relation defined relative to this new reference state, and show in Fig. 8c that these material points at $K_I = K_{max}$ (cross symbols in Fig. 8c) now follow the linear relationship with identical stiffness (E). When unloaded to $K_I = 0$ (i.e., the new reference state), all material points fully unload to $(\tilde{\varepsilon}_e, \tilde{\sigma}_e) = (0,0)$ as shown by the open circle symbol in Fig. 8c.

Since the current stress ($\tilde{\sigma}_{ij}$) and strain ($\tilde{\varepsilon}_{ij}$) measurements based on this new reference state are fully elastic at $K_I = K_{max}$, the Maxwell-Betti's reciprocal theorem is now valid and can be rewritten as (Tran et al., 2022)

$$\int_{\partial R_1} \hat{\sigma}_{ij} n_i \tilde{u}_j - \tilde{\sigma}_{ij} n_i \hat{u}_j dS = \int_{\partial R_2} \hat{\sigma}_{ij} n_i \tilde{u}_j - \tilde{\sigma}_{ij} n_i \hat{u}_j dS \tag{12}$$

Substituting (10) and (11) in (12), we obtain

$$\int_{\partial R_1} \hat{t}_2 u_2 - t_2 \hat{u}_2 dx_1 = \int_{\partial R_2} (\hat{\sigma}_{ij} \tilde{u}_j - \sigma_{ij} \hat{u}_j) n_i dS - J_R = \mathcal{M} \tag{13}$$

where $J_R = \int_R \sigma_{ij}^{res} \hat{u}_{j,i} dV + \int_{\partial R_1} \hat{t}_2 u_2^{res} dx_1$ is the reciprocity gap to account for background plasticity, where u_2^{res} is the displacement component associated with ε_{ij}^{res} at the unloaded state. The reference state displacement $\tilde{u}_j$ in (13) is obtained from the elastic strain, $\tilde{\varepsilon}_{ij}$, through the finite element derivative of shape function (B matrix) with a prescribed displacement boundary condition from (2) at the elastic remote boundary which has to be larger than the expected plane strain plastic zone size of $r_p = \sim 145D$ (Anderson, 2017). For a fully-elastic material, $J_R = 0$, $\tilde{u}_j = u_j$, which reduces (13) to (6), and we recover the original PINN formulation. Based on this augmented PINN formulation, termed as PINN–J_R, for elasto-plastic materials, which transforms (u_j, σ_{ij}) at $K_I = K_{max}$ into $(\tilde{u}_j, \tilde{\sigma}_{ij})$, we show in Fig. 9b that the extracted traction distribution, separation distribution and cohesive zone law are now in perfect agreement with ground truth data (symbols), regardless of the domain used for the measurement data (comparing the solid and dash lines).

4. Experimental Reconstruction of Crack-tip Cohesive Zone Law

The PINN–J_R approach to reconstructing the crack-tip cohesive zone law in plastically-deforming materials in Section 3.2 requires elastic strain information at both the loaded ($K_I = K_{max}$) and unloaded ($K_I = 0$) states for computations of ε_{ij}^{el} and ε_{ij}^{res}, respectively. While this information is readily available in finite element analysis, it can be challenging to obtain from traditional full-field measurement techniques such as digital image correlation (DIC). In our recent work, we have conducted both cohesive interface simulations and in situ strain measurements in a ZK60 Mg alloy in a compact-tension setup (Xie et al., 2022). Taking advantage of the high penetration capability of synchrotron X-ray diffraction (S-XRD), our experiments at Advanced Photon Source, Argonne National Laboratory allow us to probe the lattice strain field, as shown in Fig. 10a, whereas the Debye-Scherrer ring distortions can be used to obtain the directional strain and the entire in-plane strain tensor after a tensorial operation. All these strain components are elastic, and the measurements were performed at the crack tip centered about (0,0), with a beam size of 100 μm × 100 μm with a step of 100 μm which covers horizontal and vertical distances of −1.5 mm to +3.5 mm and −2 mm to +3 mm, respectively (Fig. 10a-right). These elastic strain measurements were taken at a series of load levels in a loading-unloading steady state fatigue cycle, including the load at $K_I = 250$ MPa$\sqrt{mm} = K_{max}$ and the fully unloaded configuration at $K_I = 0$ (Fig. 10a-left). Xie et. al. (2022) calculated the plastic zone size r_p to be ~0.5 mm at $K_I = K_{max}$, assuming an initial yield stress of $\sigma_y = 145$ MPa for ZK60.

Here, we use our PINN–J_R formulated in Section 3.2 to reconstruct the crack-tip traction-separation relationship of ZK60 Mg alloy (valid up to the loading of $K_I = K_{max}$) from the S-XRD-obtained elastic strain field measurements (ε_{ij}^{el}) at $K_I = K_{max}$ (Fig. 10b) and the elastic residual strain measurements (ε_{ij}^{res}) at $K_I = 0$ (Fig. 10c). First, we subtract both these strain fields to obtain $\tilde{\varepsilon}_{ij}$ in (10), taking care to average $|\tilde{\varepsilon}_{ij}|$ between the region above ($x_2 > 0$) and below ($x_2 < 0$) the crack face to obtain the expected symmetry and anti-symmetry for ($\tilde{\varepsilon}_{11}, \tilde{\varepsilon}_{22}$) and $\tilde{\gamma}_{12} = 2\tilde{\varepsilon}_{12}$, respectively,

from the imposed mode I (K_I) loading (Fig. 11a). The experimental measurement data is not accurate near the "messy" fracture process zone. Accordingly, we omit the strain data near the crack-tip and reconstruct the crack-tip cohesive zone law from $\tilde{\varepsilon}_{ij}$ data outside this zone of uncertainty. The nodes that lie along the boundary (red path in Fig. 11a) are sufficiently far away from the ~0.5 mm estimated plastic zone size, such that the displacement field at this outer boundary approximately follows the mode I K-dominant elastic regime in (2). Assuming an elastic modulus of $E = 50$ GPa and Poisson's ratio of $\nu = 0.3$ for ZK60, we obtain the displacements of the interior nodes $\tilde{u}_i$ from $\tilde{\varepsilon}_{ij}$ through the finite element derivative of shape function (B matrix), as shown in Fig. 11b.

The measurement data ($\tilde{u}_j$, $\tilde{\sigma}_{ij}$) along both ∂R_2^i and ∂R_2^{ii} in Fig. 11b are subsequently fed into our optimized PINN–J_R architecture (with $n = 3, p = 0.5$ and $n = 9, p = 0.17$) to extract the traction and separation distributions and equivalent cohesive zone law. Regardless of the path taken and the n, p combination invoked for the PINN–J_R, there is almost no discernable difference between the predicted traction distributions, as well as the predicted separation distributions (Fig. 11c), which suggests the stability and reliability of PINN–J_R. The reconstructed traction distributions increase sharply from zero to reach a peak cohesive traction $t_0 = \sim 160$ MPa centered at $x_1 \approx 0$ mm, before decreasing gradually towards a constant $t_2 = \sim 95$ MPa when $x_1 > 1.5$ mm. Similarly, the separation distributions decrease rapidly to ~ 0.0015 mm slightly ahead of the crack-tip (at $x_1 \approx 0$ mm), before tapering gradually to zero at a distance $x_1 = 2.4$ mm ahead of the crack-tip. Together, all four corresponding traction-separation relations for ZK60 exhibit a consistent, unique shape with three distinct regimes: (1) constant traction of $t_2 = \sim 95$ MPa for initial separation up to $\delta_2 = \sim 0.0015$ mm, (2) near instantaneous increase in traction to reach its peak of ~160 MPa at $\delta_2 = 0.0022$ mm, and (3) near linear (or slightly concave) softening to reach its full separation at $\delta_0 = \sim 0.009$ mm.

To validate the experimental cohesive zone laws in Fig. 11c for ZK60, we create a finite element model comprising of a uniform 100 μm × 100 μm grid of 4-noded CPE4 plane-strain elements, each element representing a single pixel in the original experimental data grid (Fig. 10b,c), with linear elastic material properties of $E = 50$ GPa, $\nu = 0.3$. We include the residual strain field ε_{ij}^{res} (Fig. 10c) as an initial stress in the finite element model (Fig. 12a) and introduce a single row of cohesive elements along $x_2 = 0$ (dash red lines) governed by the average traction-separation response predicted by PINN–J_R for $n = 3, p = 0.5$ and $n = 9, p = 0.17$ along ∂R_2^i in Fig. 11c. We subject the nodes at the far-field boundary (red path in Fig. 12a) to the same $K_I = 250$ MPa$\sqrt{\text{mm}}$ displacement boundary conditions in (2). The resulting FEM calculations in Fig. 12b correctly predicts the experimental elastic strain field ($\varepsilon_{11}^{el}, \varepsilon_{22}^{el}, \gamma_{12}^{el}$) in Fig. 10b, as further illustrated by the very comparable strain distributions along several vertical and horizontal cross-sections outside of the "messy" fracture process zone shown in Fig. 12c and 12d. The close similarity between the simulated and measured $\varepsilon_{11}^{el}, \varepsilon_{22}^{el}, \gamma_{12}^{el}$ fields suggest that our PINN–J_R correctly captures the experimental cohesive zone relationship of ZK60 up to the loading of $K_I = K_{max}$.

5. Discussions and Conclusion

Cohesive zone laws are quantitative representations of the complicated fracture process zone ahead of a crack-tip. Traditionally, the peak cohesive traction, cohesive energy, and cohesive separation have been regarded as phenomenological parameters that can be calibrated to match the crack growth response (e.g. R-curves) in experiments. However, several studies have now confirmed the correlation between the shape of the cohesive zone law and the underlying crack growth micromechanics. Constructing the full functional form of the cohesive zone law is a highly non-trivial task. Since direct measurements at the scale of the fracture process zone are challenging, one can only infer this cohesive traction versus separation relationship based on measurement data at the far-field.

Our results here demonstrate that PINNs, which constrain the cohesive tractions and separations along the crack face to satisfy the Maxwell-Betti's reciprocal theorem, can successfully construct the cohesive zone law representative of the process zone from measurement data in the far-field. While this represents a classical inverse problem which suffers from ill-conditioning, our numerical studies show that the PINN is capable of stable cohesive zone extraction. In comparison, previously-employed spectral (or field projection) methods (Chew, 2013; Cui et al., 2020; Cui and Chew, 2022; Tran et al., 2022; Noh and Chew, 2024) rely on series solutions to represent the unknown cohesive tractions and separations. The accuracy of such field projection methods depends critically on the height h of the analysis domain (Chew, 2013; Tran et al., 2022), where increasing distance of the measurement data from the cohesive interface readily leads to singularity in the inversion scheme (Willis, 1966; Chew, 2013). Higher-order series solutions are often needed to mitigate "non-periodic jumps" at the bounds of the domain in cases where a periodic series solution (e.g., Fourier series) is employed, or to capture sharp or highly localized transitions in the traction or separation distributions. The conundrum here is that these higher order terms in the series solution often cannot be accurately ascertained from field projection method because of ill-conditioning, which significantly limits the types of cohesive zone shapes that can be reconstructed. Our PINN approach is found to be remarkably stable even when the measurement data is taken at distances far from the cohesive zone (Fig. 6). It can also reconstruct with high accuracy a wide variety of cohesive zone shapes – convex, concave, trapezoidal, bilinear, polynomial, and exponential – without further optimization of the neural network, even those with large "non-periodic jumps" at the boundaries or sharp, localized transitions in the traction, separation distributions (Figs. S1 and S2 of the Supplementary Materials), and traction-separation profile (Fig. 7). In addition, our PINN approach is found to stably extract the explicit form of the cohesive zone law even in the presence of numerical noise introduced in the strain field to replicate possible disturbances in a real material (Fig. S3 of the Supplementary Materials).

More severe forms of such disturbances in the data can be corrected with an equilibrium field regularization algorithm (Hong et al. 2009, Chew et al. 2009) prior to performing the PINN.

Conservative integrals including the J- and M-integral are widely employed in forward and inverse fracture mechanics problems (Chen and Shield, 1977). In our formulation, we expand the use of conservation integrals as physics-based constraints through the enforcement of the more general Maxwell-Betti's reciprocal theorem, which is widely applicable to general interface problems, such as adhesive joints and interfaces, bio-adhesive properties of cellular structures at the nanoscale, grain boundaries, etc. (Zhu et al., 2000; Chew et al., 2005; Desai et al., 2016; Jiang et al., 2023; Wei et al., 2023). In the absence of noise in the numerical and experimental data, the obtained cohesive traction and separation distributions will be unique if they are constrained to satisfy the reciprocal theorem for an infinite number of admissible auxiliary fields. Here, we carefully design two classes of sinusoidal-based auxiliary fields, each governed by a wavenumber k, which allows us to generate an entire series of unique auxiliary fields. Ideally, one could constrain the PINN to satisfy the reciprocal theorem for a large number of such auxiliary fields (i.e., large number of wavenumbers n). In practice, however, any small gains in ensuring solution uniqueness (through the implementation of large n) is offset by numerical errors which increases with n. This effectively places a limit on n in our PINN, as seen from the similar traction-separation predictions between $n = 3$ and $n = 9$ in Fig. 7.

While the Maxwell-Betti's reciprocal theorem strictly limits it to elastic problems, we have reformulated the reciprocal theorem following (Tran et al., 2022) to treat the background plasticity as an initial elastic residual stress, which permits the use of the reciprocal theorem with a reciprocity gap to account for this residual elastic stress. Our modified reciprocal theorem is applicable for any elasto-plastic material that exhibits linear unloading and reloading along the same path. Since we explicitly delineate the cohesive zone from the background plasticity, our extracted cohesive zone law only embeds the underlying crack growth micromechanics within the narrow process zone and

thus represents the intrinsic fracture response of the material. This decoupling between background plasticity and process zone damage is applicable to a wide variety of interface problems, including the delineation between plasticity within the grain interior and the deformation mechanics at the grain boundary (Wei and Anand, 2004), or delineation between matrix material deformation and interfacial failure in nanotube-reinforced composites (Bagchi et al., 2018).

We have applied this augmented PINN–J_R to inversely reconstruct the cohesive zone law from both the elastic strain fields at the current deformed state and the residual elastic strain fields after unloading obtained from S-XRD for a ZK60 Mg alloy. We obtain a unique cohesive zone law relation comprising of a "Dugdale" type regime characterized by constant traction at small separations (presumably associated with damage initiation due to twinning (Grilli et al., 2022; Xie et al., 2022)), a sharp increase in traction with further separation, followed by a linear softening regime. By implementing this experimentally-obtained cohesive zone law in FEM, we have successfully recovered the strain fields from S-XRD, validating our PINN approach. This extracted cohesive zone law is associated with a single loading stage of a fatigue crack (valid from $K_I = 0$ to K_{max}, and thus might not be representative of the full cohesive zone law for monotonic fracture of ZK60. However, one can certainly extend this analysis to the higher K_I to obtain the full cohesive zone law for crack growth, or to different loading and unloading stages within a single steady-state fatigue cycle for construction of the cohesive zone law for fatigue crack growth with unloading-reloading hysteresis.

In summary, we have introduced a new PINN capable of reconstructing the interfacial tractions and separations in both elastic and elasto-plastic materials from far-field measurement data. Compared to prior field projection methods, this neural network approach is remarkably stable even when the cohesive zone reconstruction is based on measurement data far from the crack face. Our PINN's ability to capture highly localized details of the traction-separation relation, in concert with S-XRD measurements, renders it suitable for providing rich fundamental insights into the crack

growth micromechanics under complex loading conditions. Although we have only applied this PINN approach towards rate-independent, elasto-plastic problems under mode I loading, we remark that this PINN approach is very general, and can be easily extended to mixed-mode loading by modifying the PINN outputs and the auxiliary fields to include the shear traction/separation contributions, or to rate-dependent, temperature-dependent or even stochastic crack growth problems (Wei, 2014) by incorporating the relevant reciprocal theorem (e.g., Shivay and Mukhopadhyay, 2021). These are subjects of future work.

Table 1: Hyperparameter testing of the PINN. *Shaded*: locally optimal architecture for each systematic parametric variation. *Bold*: final optimized architecture.

Hyper-parameters	Neural network structure		Learning rate, l_r	Weight contribution			Activation function	Error	
	Hidden layers	Nodes per hidden layer		w_1	w_2	w_3		$\min(L_s)/w_3$ $(\times 10^{-12})$	RMSE
Neural network structure	10	10	0.0001	1	1	10000	ELU	3.13	0.069
	30	10	0.0001	1	1	10000	ELU	2.87	0.098
	40	10	0.0001	1	1	10000	ELU	130810	0.389
	10	15	0.0001	1	1	10000	ELU	1	0.042
	10	20	0.0001	1	1	10000	ELU	0.94	0.078
	20	20	0.0001	1	1	10000	ELU	0.73	0.045
	40	20	0.0001	1	1	10000	ELU	130542	0.389
	10	30	0.0001	1	1	10000	ELU	0.89	0.023
	10	40	0.0001	1	1	10000	ELU	1.19	0.070
	10	80	0.0001	1	1	10000	ELU	1.43	0.076
	20	80	0.0001	1	1	10000	ELU	0.86	0.119
Learning rate	10	30	0.01	1	1	10000	ELU	273.7	0.264
	10	30	0.005	1	1	10000	ELU	75.4	0.199
	10	30	0.001	1	1	10000	ELU	2.05	0.063
	10	30	0.0005	1	1	10000	ELU	3.13	0.101
	10	30	0.00005	1	1	10000	ELU	0.75	0.044
	10	30	0.00003	1	1	10000	ELU	0.82	0.040
	10	30	0.00002	1	1	10000	ELU	0.61	0.040
	10	30	0.00001	1	1	10000	ELU	2.12	0.043
Weight contribution	10	30	0.00002	0	1	10000	ELU	1.85	0.196
	10	30	0.00002	1	0	10000	ELU	0.62	0.043
	10	30	0.00002	1	1	100000	ELU	0.68	0.071
	10	30	0.00002	1	1	10000	ELU	0.61	0.040
	10	30	0.00002	1	1	1000	ELU	11.89	0.303
	10	30	0.00002	1	1	10	ELU	268.96	0.263
Activation function	**10**	**30**	**0.00002**	**1**	**1**	**10000**	**ELU**	**0.61**	**0.040**
	10	30	0.00002	1	1	10000	TANH	0.70	0.068
	10	30	0.00002	1	1	10000	RELU	1.05	0.078

Acknowledgements

The authors acknowledge the support provided by NASA through the Joint Advanced Propulsion Institute, a NASA Space Technology Research Institute, under grant number 80NSSC21K1118, as

well as the support provided by National Science Foundation under Grant Nos: NSF-CMMI-2009684, NSF-CMMI-2425707, NSF-DMR-1809640, NSF-DMR-1809696, and NSF-DMR-2406764. The use of the Advanced Cyberinfrastructure Coordination Ecosystem: Services & Support (ACCESS), through allocations MAT230069, MAT210031, and MAT230055, and TACC Frontera through allocation MSS22006, is gratefully acknowledged.

Appendix A: Analytical auxiliary fields

The analytical full-field solution for a sinusoidal shear traction $t_1(x_1) = -\sigma_0 e^{\mathbf{i}\frac{2k\pi}{L}x_1}$ of amplitude σ_0 with period L and wavelength k on an upper elastic half-space ($x_2 > 0$) is well-established

$$\begin{aligned}
\sigma_{11} &= -\mathbf{i}\sigma_0\left(2 - \frac{2k\pi x_2}{L}\right)e^{\frac{2k\pi}{L}(\mathbf{i}x_1 - x_2)} \\
\sigma_{22} &= -\mathbf{i}\sigma_0\frac{2k\pi x_2}{L}e^{\frac{2k\pi}{L}(\mathbf{i}x_1 - x_2)} \\
\sigma_{12} &= \sigma_0\left(1 - \frac{2k\pi x_2}{L}\right)e^{\frac{2k\pi}{L}(\mathbf{i}x_1 - x_2)} \\
u_1 &= \frac{L}{2k\pi}(1+\nu)\frac{\sigma_0}{E}\left(-2(1-\nu) + \frac{2k\pi x_2}{L}\right)e^{\frac{2k\pi}{L}(\mathbf{i}x_1 - x_2)} \\
u_2 &= \frac{L}{2k\pi}(1+\nu)\frac{\sigma_0}{E}\left(\mathbf{i}(1-2\nu) + \mathbf{i}\frac{2k\pi x_2}{L}\right)e^{\frac{2k\pi}{L}(\mathbf{i}x_1 - x_2)}
\end{aligned} \tag{A1}$$

Observe that $\sigma_{12}(x_1) = 0$ and $\sigma_{22}(x_1) = -\mathbf{i}e^{-1}\sigma_0 e^{\mathbf{i}\frac{2k\pi}{L}x_1}$ at $x_2 = \frac{L}{2k\pi}$, inferring that the solution for a normal sinusoidal surface traction $t_2(x_1) = -\sigma_0 e^{\mathbf{i}\frac{2k\pi}{L}x_1}$ can be obtained by simply substituting $\sigma_0 \to -\mathbf{i}e\sigma_0$ and $x_2 \to x_2 + \frac{L}{2\pi k}$ in (A1)

$$\begin{aligned}
\sigma_{11} &= \sigma_0\left(1 - \frac{2k\pi x_2}{L}\right)e^{\frac{2k\pi}{L}(\mathbf{i}x_1 - x_2)} \\
\sigma_{22} &= \sigma_0\left(1 + \frac{2k\pi x_2}{L}\right)e^{\frac{2k\pi}{L}(\mathbf{i}x_1 - x_2)} \\
\sigma_{12} &= -\mathbf{i}\sigma_0\frac{2k\pi x_2}{L}e^{\frac{2k\pi}{L}(\mathbf{i}x_1 - x_2)} \\
u_1 &= \frac{L}{2k\pi}(1+\nu)\frac{\sigma_0}{E}\left(\mathbf{i}(-1+2\nu) + \mathbf{i}\frac{2k\pi x_2}{L}\right)e^{\frac{2k\pi}{L}(\mathbf{i}x_1 - x_2)} \\
u_2 &= \frac{L}{2k\pi}(1+\nu)\frac{\sigma_0}{E}\left(-2(1-\nu) - \frac{2k\pi x_2}{L}\right)e^{\frac{2k\pi}{L}(\mathbf{i}x_1 - x_2)}
\end{aligned} \tag{A2}$$

We introduce two classes of analytical auxiliary fields for the Maxwell-Betti's reciprocal theorem outlined in Fig. 2b. The first class is a full-field solution $\hat{S}_1(\hat{\sigma}_{ij}, \hat{u}_i)$ of an elastic half-space subjected to periodic sin or cos distributions of normal tractions $\hat{t}_2(x_1) = -\sigma_0 e^{\mathbf{i}\frac{2k\pi}{L}x_1}$, explicitly provided in (A2). The second class is a field solution $\hat{S}_2(\hat{\sigma}_{ij}, \hat{u}_i)$ with traction free surface but non-zero periodic displacements, obtained by superposing two separate linear elastic fields using principle of superposition outlined below (Fig. A1).

To obtain $\hat{S}_2(\hat{\sigma}_{ij}, \hat{u}_i)$, we first apply a normal traction $\sigma_0 e^{\mathbf{i}\frac{2k\pi}{L}x_1}$ on the surface located at $x_2 = H$ of a lower half-space, resulting in the following field solution obtained by substituting $x_2 \to (H - x_2)$, $\sigma_{11} \to -\sigma_{11}, \sigma_{22} \to -\sigma_{22}, u_2 \to -u_2$ in (A2)

$$
\begin{aligned}
\sigma_{11} &= \sigma_0 \left(1 + \tfrac{2k\pi(x_2-H)}{L}\right) e^{\frac{2k\pi}{L}(\mathbf{i}x_1 + x_2 - H)} \\
\sigma_{22} &= -\sigma_0 \left(1 - \tfrac{2k\pi(x_2-H)}{L}\right) e^{\frac{2k\pi}{L}(\mathbf{i}x_1 + x_2 - H)} \\
\sigma_{12} &= \mathbf{i}\sigma_0 \tfrac{2k\pi(x_2-H)}{L} e^{\frac{2k\pi}{L}(\mathbf{i}x_1 + x_2 - H)} \\
u_1 &= \tfrac{L}{2k\pi}(1+\nu)\tfrac{\sigma_0}{E}\left(\mathbf{i}(-1+2\nu) - \mathbf{i}\tfrac{2k\pi(x_2-H)}{L}\right) e^{\frac{2k\pi}{L}(\mathbf{i}x_1 + x_2 - H)} \\
u_2 &= \tfrac{L}{2k\pi}(1+\nu)\tfrac{\sigma_0}{E}\left(2(1-\nu) - \tfrac{2k\pi(x_2-H)}{L}\right) e^{\frac{2k\pi}{L}(\mathbf{i}x_1 + x_2 - H)}
\end{aligned}
\tag{A3}
$$

The fields in this lower half-space decay exponentially with x_2, but we still have a sinusoidally varying $(\hat{\sigma}_{12}, \hat{\sigma}_{22})$ field along $x_2 = 0$ (Fig. A1a). We subsequently impose a combination of shear and normal tractions $\hat{t}_i$ along the $x_2 = 0$ surface of an upper half space, with magnitudes resulting in $-\hat{\sigma}_{12}$ and $-\hat{\sigma}_{22}$ respectively along $x_2 = 0$ (Fig. A1b). The field solution of this upper half space can be obtained from a combination of (A1) and (A2). Finally, we superpose the field solutions of both this lower (Fig. A1a) and upper half space (Fig. A1b) to obtain $\hat{S}_2$ (Fig. A1c), which has a traction-free surface boundary but with non-zero displacements along $x_2 = 0$.

The real and imaginary portion of each class of auxiliary field corresponds to two independent auxiliary field solutions from imposing a cos or sin distribution (imaginary or real part, respectively)

of surface tractions ($x_2 = 0$ for $\hat{S}_1$ in Fig. 2a and $x_2 = H$ for $\hat{S}_2$ in Fig. A1). Together, both classes of auxiliary fields, $\hat{S}_1$ and $\hat{S}_2$, provides a total of four independent auxiliary fields for each wavenumber k. Considering the application of n wavenumbers, i.e., k ranging from 1 to n, we have a total of $4n$ independent auxiliary fields to be used in the Maxwell-Betti's reciprocal theorem.

References:

Akhavan-Safar, A., Marques, E.A.S., Carbas, R.J.C., da Silva, L.F.M., 2022. Cohesive Zone Modelling-CZM, in: Akhavan-Safar, A., Marques, E.A.S., Carbas, R.J.C., da Silva, L.F.M. (Eds.), Cohesive Zone Modelling for Fatigue Life Analysis of Adhesive Joints, SpringerBriefs in Applied Sciences and Technology. Springer International Publishing, Cham, pp. 19–42. https://doi.org/10.1007/978-3-030-93142-1_2

Alfano, G., 2006. On the influence of the shape of the interface law on the application of cohesive-zone models. Composites Science and Technology, Advances in statics and dynamics of delamination 66, 723–730. https://doi.org/10.1016/j.compscitech.2004.12.024

Alfano, M., Furgiuele, F., Leonardi, A., Maletta, C., Paulino, G.H., 2009. Mode I fracture of adhesive joints using tailored cohesive zone models. Int J Fract 157, 193–204. https://doi.org/10.1007/s10704-008-9293-4

Allix, O., Corigliano, A., 1996. Modeling and simulation of crack propagation in mixed-modes interlaminar fracture specimens. Int J Fract 77, 111–140. https://doi.org/10.1007/BF00037233

Anderson, T.L., 2017. Fracture Mechanics: Fundamentals and Applications, Fourth Edition. CRC Press.

Bagchi, S., Harpale, A., Chew, H.B., 2018. Interfacial load transfer mechanisms in carbon nanotube-polymer nanocomposites. Proceedings of the Royal Society A 474, 20170705.

Campilho, R.D.S.G., Banea, M.D., Neto, J.A.B.P., da Silva, L.F.M., 2013. Modelling adhesive joints with cohesive zone models: effect of the cohesive law shape of the adhesive layer. International Journal of Adhesion and Adhesives 44, 48–56. https://doi.org/10.1016/j.ijadhadh.2013.02.006

Chandra, N., Li, H., Shet, C., Ghonem, H., 2002. Some issues in the application of cohesive zone models for metal–ceramic interfaces. International Journal of Solids and Structures 39, 2827–2855. https://doi.org/10.1016/S0020-7683(02)00149-X

Chen, C.R., Kolednik, O., Scheider, I., Siegmund, T., Tatschl, A., Fischer, F.D., 2003. On the determination of the cohesive zone parameters for the modeling of micro-ductile crack growth in thick specimens. International Journal of Fracture 120, 517–536. https://doi.org/10.1023/A:1025426121928

Chen, F.H.K., Shield, R.T., 1977. Conservation laws in elasticity of the J-integral type. Journal of Applied Mathematics and Physics (ZAMP) 28, 1–22. https://doi.org/10.1007/BF01590704

Chew, H.B., 2014. Cohesive zone laws for fatigue crack growth: Numerical field projection of the micromechanical damage process in an elasto-plastic medium. International Journal of Solids and Structures 51, 1410–1420. https://doi.org/10.1016/j.ijsolstr.2013.12.033

Chew, H.B., 2013. Inverse extraction of interfacial tractions from elastic and elasto-plastic far-fields by nonlinear field projection. Journal of the Mechanics and Physics of Solids 61, 131–144. https://doi.org/10.1016/j.jmps.2012.08.007

Chew, H.B., Guo, T.F., Cheng, L., 2005. Vapor pressure and residual stress effects on failure of an adhesive film. International Journal of Solids and Structures 42, 4795–4810. https://doi.org/10.1016/j.ijsolstr.2005.01.012

Chew, H.B., Hong, S., Kim, K.-S., 2009. Cohesive zone laws for void growth — II. Numerical field projection of elasto-plastic fracture processes with vapor pressure. Journal of the Mechanics and Physics of Solids 57, 1374–1390. https://doi.org/10.1016/j.jmps.2009.04.001

Cox, B.N., Marshall, D.B., 1991. The determination of crack bridging forces. International Journal of Fracture, 49, 159-176.

Cui, Y., Chew, H.B., 2022. Machine-Learning Prediction of Atomistic Stress along Grain Boundaries. Acta Materialia 222, 117387. https://doi.org/10.1016/j.actamat.2021.117387
Cui, Y., Gao, Y.F., Chew, H.B., 2020. Two-scale porosity effects on cohesive crack growth in a ductile media. International Journal of Solids and Structures 200–201, 188–197. https://doi.org/10.1016/j.ijsolstr.2020.04.035
Cuomo, S., Di Cola, V.S., Giampaolo, F., Rozza, G., Raissi, M., Piccialli, F., 2022. Scientific Machine Learning Through Physics–Informed Neural Networks: Where we are and What's Next. J Sci Comput 92, 88. https://doi.org/10.1007/s10915-022-01939-z
Da Silva, I.N., Hernane Spatti, D., Andrade Flauzino, R., Liboni, L.H.B., Dos Reis Alves, S.F., 2017. Artificial Neural Networks. Springer International Publishing, Cham. https://doi.org/10.1007/978-3-319-43162-8
Desai, C.K., Basu, S., Parameswaran, V., 2016. Determination of Traction Separation Law for Interfacial Failure in Adhesive Joints at Different Loading Rates. The Journal of Adhesion 92, 819–839. https://doi.org/10.1080/00218464.2015.1046986
Diao, Y., Yang, J., Zhang, Y., Zhang, D., Du, Y., 2023. Solving multi-material problems in solid mechanics using physics-informed neural networks based on domain decomposition technology. Computer Methods in Applied Mechanics and Engineering 413, 116120. https://doi.org/10.1016/j.cma.2023.116120
Dugdale, D.S., 1960. Yielding of steel sheets containing slits. Journal of the Mechanics and Physics of Solids 8, 100–104. https://doi.org/10.1016/0022-5096(60)90013-2
Elices, M., Guinea, G.V., Gómez, J., Planas, J., 2002. The cohesive zone model: advantages, limitations and challenges. Engineering Fracture Mechanics 69, 137–163. https://doi.org/10.1016/S0013-7944(01)00083-2
Gao, Y., 2016. Deformation fields near a steady fatigue crack with anisotropic plasticity. Extreme Mechanics Letters 6, 45–51. https://doi.org/10.1016/j.eml.2015.11.006
Gao, Y.F., Bower, A.F., 2004. A simple technique for avoiding convergence problems in finite element simulations of crack nucleation and growth on cohesive interfaces. Modelling and Simulation in Materials Science and Engineering 12, 453–463. https://doi.org/10.1088/0965-0393/12/3/007
García-Cervera, C.J., Kessler, M., Periago, F., 2023. Control of Partial Differential Equations via Physics-Informed Neural Networks. J Optim Theory Appl 196, 391–414. https://doi.org/10.1007/s10957-022-02100-4
Gladysz, G.M., Chawla, K.K., 2020. Voids in Materials: From Unavoidable Defects to Designed Cellular Materials. Elsevier.
Grilli, N., Cocks, A.C.F., Tarleton, E., 2022. Modelling the nucleation and propagation of cracks at twin boundaries. Int J Fract 233, 17–38. https://doi.org/10.1007/s10704-021-00606-y
Guo, Z.K., Kobayashi, A.S., Hay, J.C., White, K.W., 1999. Fracture process zone modeling of monolithic Al2O3. Engineering Fracture Mechanics 63, 115–129. https://doi.org/10.1016/S0013-7944(99)00030-2
Gustafson, P.A., Waas, A.M., 2009. The influence of adhesive constitutive parameters in cohesive zone finite element models of adhesively bonded joints. International Journal of Solids and Structures, Special Issue in Honor of Professor Liviu Librescu 46, 2201–2215. https://doi.org/10.1016/j.ijsolstr.2008.11.016
He, M., Xin, K., 2011. Separation work analysis of cohesive law and consistently coupled cohesive law. Appl. Math. Mech.-Engl. Ed. 32, 1437–1446. https://doi.org/10.1007/s10483-011-1513-x

Heidari-Rarani, M., Ghasemi, A.R., 2017. Appropriate shape of cohesive zone model for delamination propagation in ENF specimens with R-curve effects. Theoretical and Applied Fracture Mechanics 90, 174–181. https://doi.org/10.1016/j.tafmec.2017.04.009

Hillerborg, A., Modéer, M., Petersson, P.-E., 1976. Analysis of crack formation and crack growth in concrete by means of fracture mechanics and finite elements. Cement and Concrete Research 6, 773–781. https://doi.org/10.1016/0008-8846(76)90007-7

Hong, S., Chew, H.B., Kim, K.-S., 2009. Cohesive-zone laws for void growth — I. Experimental field projection of crack-tip crazing in glassy polymers. Journal of the Mechanics and Physics of Solids 57, 1357–1373. https://doi.org/10.1016/j.jmps.2009.04.003

Hong, S., Kim, K.-S., 2003. Extraction of cohesive-zone laws from elastic far-fields of a cohesive crack tip: a field projection method. Journal of the Mechanics and Physics of Solids 51, 1267–1286. https://doi.org/10.1016/S0022-5096(03)00023-1

Hutchinson, J.W., Evans, A.G., 2000. Mechanics of materials: top-down approaches to fracture. Acta Materialia 48, 125–135. https://doi.org/10.1016/S1359-6454(99)00291-8

Jemblie, L., Olden, V., Akselsen, O.M., 2017. A review of cohesive zone modelling as an approach for numerically assessing hydrogen embrittlement of steel structures. Philosophical Transactions of the Royal Society A: Mathematical, Physical and Engineering Sciences 375, 20160411. https://doi.org/10.1098/rsta.2016.0411

Jiang, Y., Li, N., Liu, Z., Yi, C., Zhou, H., Park, C., Fay, C.C., Deng, J., Chew, H.B., Ke, C., 2023a. Exceptionally strong boron nitride nanotube aluminum composite interfaces. Extreme Mechanics Letters 59, 101952. https://doi.org/10.1016/j.eml.2022.101952

Jiang, Y., Sridhar, S., Liu, Z., Wang, D., Zhou, H., Deng, J., Chew, H.B., Ke, C., 2023b. The interplay of intra- and inter-layer interactions in bending rigidity of ultrathin 2D materials. Applied Physics Letters 122, 153101. https://doi.org/10.1063/5.0146065

Kafkalidis, M.S., Thouless, M.D., 2002. The effects of geometry and material properties on the fracture of single lap-shear joints. International Journal of Solids and Structures 39, 4367–4383. https://doi.org/10.1016/S0020-7683(02)00344-X

Kim, H.-G., Chew, H.B., Kim, K.-S., 2012. Inverse extraction of cohesive zone laws by field projection method using numerical auxiliary fields. International Journal for Numerical Methods in Engineering 91, 516–530. https://doi.org/10.1002/nme.4281

Lélias, G., Paroissien, E., Lachaud, F., Morlier, J., 2019. Experimental characterization of cohesive zone models for thin adhesive layers loaded in mode I, mode II, and mixed-mode I/II by the use of a direct method. International Journal of Solids and Structures 158, 90–115. https://doi.org/10.1016/j.ijsolstr.2018.09.005

Li, H., Chandra, N., 2003. Analysis of crack growth and crack-tip plasticity in ductile materials using cohesive zone models. International Journal of Plasticity 19, 849–882. https://doi.org/10.1016/S0749-6419(02)00008-6

Li, N., Dmuchowski, C.M., Jiang, Y., Yi, C., Gou, F., Deng, J., Ke, C., Chew, H.B., 2022. Sliding energy landscape governs interfacial failure of nanotube-reinforced ceramic nanocomposites. Scripta Materialia 210, 114413. https://doi.org/10.1016/j.scriptamat.2021.114413

Li, R., Chew, H.B., 2017. Grain boundary traction signatures: Quantifying the asymmetrical dislocation emission processes under tension and compression. Journal of the Mechanics and Physics of Solids 103, 142–154. https://doi.org/10.1016/j.jmps.2017.03.009

Li, R., Chew, H.B., 2016. Grain Boundary Traction Signatures: Quantitative Predictors of Dislocation Emission. Phys. Rev. Lett. 117, 085502. https://doi.org/10.1103/PhysRevLett.117.085502

Li, Z., Li, X., Chen, Y., Zhang, C., 2023. A mechanics-informed machine learning approach for modeling the elastoplastic behavior of fiber-reinforced composites. Composite Structures 323, 117473. https://doi.org/10.1016/j.compstruct.2023.117473
Liu, S., Shin, Y.C., 2019. Additive manufacturing of Ti6Al4V alloy: A review. Materials & Design 164, 107552. https://doi.org/10.1016/j.matdes.2018.107552
Mangal, A., Holm, E.A., 2019. Applied machine learning to predict stress hotspots II: Hexagonal close packed materials. International Journal of Plasticity 114, 1–14. https://doi.org/10.1016/j.ijplas.2018.08.003
Mangal, A., Holm, E.A., 2018. Applied machine learning to predict stress hotspots I: Face centered cubic materials. International Journal of Plasticity 111, 122–134. https://doi.org/10.1016/j.ijplas.2018.07.013
Muro-Barrios, R., Cui, Y., Lambros, J., Chew, H.B., 2022. Dual-scale porosity effects on crack growth in additively manufactured metals: 3D ductile fracture models. Journal of the Mechanics and Physics of Solids 159, 104727. https://doi.org/10.1016/j.jmps.2021.104727
Noh, W., Chew, H.B., 2024. Dislocation descriptors of low and high angle grain boundaries with convolutional neural networks. Extreme Mechanics Letters 68, 102138. https://doi.org/10.1016/j.eml.2024.102138
Olden, V., Thaulow, C., Johnsen, R., Østby, E., Berstad, T., 2008. Application of hydrogen influenced cohesive laws in the prediction of hydrogen induced stress cracking in 25%Cr duplex stainless steel. Engineering Fracture Mechanics 75, 2333–2351. https://doi.org/10.1016/j.engfracmech.2007.09.003
Perera, R., Agrawal, V., 2023. Dynamic and adaptive mesh-based graph neural network framework for simulating displacement and crack fields in phase field models. Mechanics of Materials 186, 104789. https://doi.org/10.1016/j.mechmat.2023.104789
Pierron, F., Lo, Y.-L., 2008. Inverse Problems in Experimental Mechanics. Exp Mech 48, 379–379. https://doi.org/10.1007/s11340-008-9160-2
Pierson, K., Rahman, A., Spear, A.D., 2019. Predicting Microstructure-Sensitive Fatigue-Crack Path in 3D Using a Machine Learning Framework. JOM 71, 2680–2694. https://doi.org/10.1007/s11837-019-03572-y
Rodriguez-Torrado, R., Ruiz, P., Cueto-Felgueroso, L., Green, M.C., Friesen, T., Matringe, S., Togelius, J., 2022. Physics-informed attention-based neural network for hyperbolic partial differential equations: application to the Buckley–Leverett problem. Sci Rep 12, 7557. https://doi.org/10.1038/s41598-022-11058-2
Rowe, P., Deringer, V.L., Gasparotto, P., Csányi, G., Michaelides, A., 2020. An Accurate and Transferable Machine Learning Potential for Carbon. J. Chem. Phys. 153, 034702. https://doi.org/10.1063/5.0005084
Seo, J., 2024. Solving real-world optimization tasks using physics-informed neural computing. Sci Rep 14, 202. https://doi.org/10.1038/s41598-023-49977-3
Shaidu, Y., Küçükbenli, E., Lot, R., Pellegrini, F., Kaxiras, E., de Gironcoli, S., 2021. A systematic approach to generating accurate neural network potentials: the case of carbon. npj Comput Mater 7, 52. https://doi.org/10.1038/s41524-021-00508-6
Shalev-Shwartz, S., Ben-David, S., 2014. Understanding Machine Learning: From Theory to Algorithms. Cambridge University Press, Cambridge. https://doi.org/10.1017/CBO9781107298019
Shivay, O.N., Mukhopadhyay, S., 2021. Variational principle and reciprocity theorem on the temperature-rate-dependent poro-thermoelasticity theory. Acta Mech 232, 3655–3667. https://doi.org/10.1007/s00707-021-02996-5
Smith, M., 2009. ABAQUS/Standard User's Manual, Version 6.9.

Sørensen, B.F., Jacobsen, T.K., 2003. Determination of cohesive laws by the J integral approach. Engineering Fracture Mechanics 70(14), 1841-1858.
Tao, C., Zhang, C., Ji, H., Qiu, J., 2023. A Paris-law-informed neural fatigue cohesive model and its application to open-hole composite laminates. International Journal of Solids and Structures 267, 112158. https://doi.org/10.1016/j.ijsolstr.2023.112158
Tran, H., Chew, H.B., 2022. Cohesive Zone Interpretations of Phase-Field Fracture Models. Journal of Applied Mechanics 89. https://doi.org/10.1115/1.4055660
Tran, H., Gao, Y.F., Chew, H.B., 2022. An inverse method to reconstruct crack-tip cohesive zone laws for fatigue by numerical field projection. International Journal of Solids and Structures 239–240, 111435. https://doi.org/10.1016/j.ijsolstr.2022.111435
Tvergaard, V., Hutchinson, J.W., 1992. The relation between crack growth resistance and fracture process parameters in elastic-plastic solids. Journal of the Mechanics and Physics of Solids 40, 1377–1397. https://doi.org/10.1016/0022-5096(92)90020-3
VanSickle, R., Foehring, D., Chew, H.B., Lambros, J., 2020. Microstructure effects on fatigue crack growth in additively manufactured Ti–6Al–4V. Materials Science and Engineering: A 795, 139993. https://doi.org/10.1016/j.msea.2020.139993
Wang, J., Zhu, B., Hui, C.-Y., Zehnder, A.T., 2023. Determination of material parameters in constitutive models using adaptive neural network machine learning. Journal of the Mechanics and Physics of Solids 177, 105324. https://doi.org/10.1016/j.jmps.2023.105324
Wei, C., Zhang, J., Liechti, K.M., Wu, C., 2023. Data driven modeling of interfacial traction–separation relations using a thermodynamically consistent neural network. Computer Methods in Applied Mechanics and Engineering 404, 115826. https://doi.org/10.1016/j.cma.2022.115826
Wei, Y.J., Anand, L., 2004. Grain-boundary sliding and separation in polycrystalline metals: application to nanocrystalline fcc metals. Journal of the Mechanics and Physics of Solids 52, 2587–2616. https://doi.org/10.1016/j.jmps.2004.04.006
Willis, J.R., 1966. Hertzian contact of anisotropic bodies. Journal of the Mechanics and Physics of Solids 14, 163–176. https://doi.org/10.1016/0022-5096(66)90036-6
Wei, Y., 2014. A stochastic description on the traction-separation law of an interface with non-covalent bonding. Journal of the Mechanics and Physics of Solids 70, 227–241. https://doi.org/10.1016/j.jmps.2014.05.014
Worthington, M., Chew, H.B., 2023. Crack path predictions in heterogeneous media by machine learning. Journal of the Mechanics and Physics of Solids 172, 105188. https://doi.org/10.1016/j.jmps.2022.105188
Xie, D., Zhang, W., Lyu, Z., Liaw, P.K., Tran, H., Chew, H.B., Wei, Y., Ren, Y., Gao, Y., 2022. Plastic anisotropy and twin distributions near the fatigue crack tip of textured Mg alloys from in situ synchrotron X-ray diffraction measurements and multiscale mechanics modeling. Journal of the Mechanics and Physics of Solids 165, 104936. https://doi.org/10.1016/j.jmps.2022.104936
Xu, X.-P., Needleman, A., 1993. Void nucleation by inclusion debonding in a crystal matrix. Modelling Simul. Mater. Sci. Eng. 1, 111. https://doi.org/10.1088/0965-0393/1/2/001
Zhang, Y., Li, Q.-J., Zhu, T., Li, J., 2022. Learning constitutive relations of plasticity using neural networks and full-field data. Extreme Mechanics Letters 52, 101645. https://doi.org/10.1016/j.eml.2022.101645
Zhu, C., Bao, G., Wang, N., 2000. Cell Mechanics: Mechanical Response, Cell Adhesion, and Molecular Deformation. Annual Review of Biomedical Engineering 2, 189–226. https://doi.org/10.1146/annurev.bioeng.2.1.189

Figure Captions

Figure 1: (**a**) Schematic of the small-scale yielding model with a centerline crack, subjected to remote mode I (K_I) loading, with a cohesive interface (dashed red line) in front of the crack tip located at $x_1 = x_2 = 0$. (**b**) Schematic of a cohesive zone, and a prescribed normal traction (t_2)-separation (δ_2) relationship. (**c**) Finite element mesh of the small-scale yielding model. (**d**) Close-up view of the highly-refined finite element mesh (green box) of uniformly sized $D \times D$ elements surrounding the initial crack tip (symbol 'x').

Figure 2: (**a**) Physics-Informed Neural Network (PINN) architecture for the reconstruction of the traction ($\mathbf{T_2}$) and separation distributions ($\mathbf{D_2}$) along the cohesive zone ($\mathbf{X_1}$) from far-field measurement data, subjected to physical and mechanistic constraints enforced by a loss function. (**b**) Schematic depicting the real field (S) and two classes of auxiliary fields ($\hat{S}_1, \hat{S}_2$) of the Maxwell-Betti's reciprocal theorem, which constitutes the primary constraint (L_3) linking measurement data along ∂R_2 (blue) to traction-separation predictions along ∂R_1 (red).

Figure 3: Hyperparameter studies on the network structure (**a**), learning rate (**b**), weights contribution of the loss function (**c**), and choice of activation function (**d**), depicting the PINN-predicted (lines) versus actual (symbols) exponential cohesive zone law; '*' supercript: locally optimal hyperparameters.

Figure 4: Weighted loss evolution (*left*) and convergence of the predicted exponential cohesive zone law with training epochs (lines, *right*) to ground truth data (symbols, *right*) for varying proportion (p) of terms enforced per epoch out of a fixed total number of constraints ($4n = 28$) in the reciprocal theorem.

Figure 5: Predicted exponential cohesive zone law (lines) versus ground truth data (symbols) for different (n, p) combinations in the reciprocal theorem.

Figure 6: Domain size effects (h/D) on the predicted exponential cohesive zone law (lines) versus ground truth data (symbols) for different (n, p) combinations in the reciprocal theorem.

Figure 7: Predicted (lines) versus ground truth data (symbols) for different functional forms of the cohesive zone law.

Figure 8: (**a**) Von Mises stress contours (σ_e/E) at the current loading $K_I = K_{max}$ and after unloading (from K_{max}) to $K_I = 0$. (**b**) Von Mises stress (σ_e/E) versus equivalent strain (ε_e) for material points 1-8 in (**a**) with the undeformed state ($\sigma_e = \varepsilon_e = 0$, circle symbol) as the reference configuration. (**c**) Von Mises stress ($\tilde{\sigma}_e/E$) versus equivalent strain ($\tilde{\varepsilon}_e$) for material points 1-8 in (**a**), taking the fully unloaded material ($K_I = 0$, circle symbol) as the reference configuration.

Figure 9: Traction distribution, separation distribution, and the cohesive zone law predicted by PINN (lines) from measurement data along two paths ($\partial R_2^i; \partial R_2^{ii}$) versus actual ground truth data (circle symbols). (**a**) Original PINN formulation for linear-elastic materials. (**b**) Augmented PINN formulation (PINN–J_R) to account for plastically deforming background material.

Figure 10: (**a**) Schematic of the diffraction setup for strain mapping measurement of a fatigue crack in a CT specimen using S-XRD, with mapping area in red dash square (Xie et. al., 2022). (**b,c**) Elastic

strain measurement (ε_{11}^{el}, $\varepsilon_{22}^{el}, \gamma_{12}^{el} = 2\varepsilon_{12}^{el}$) from S-XRD at the last fatigue cycle, where the crack is fully unloaded from $K_I = K_{max}$ (**b**) to $K_I = 0$ (**c**).

Figure 11: (**a,b**) Postprocessed S-XRD experiment elastic strain measurement ($\tilde{\varepsilon}_{11}, \tilde{\varepsilon}_{22}, \tilde{\gamma}_{12} = 2\tilde{\varepsilon}_{12}$) (**a**) and numerically reconstructed displacement field ($\tilde{u}_1, \tilde{u}_2$) with assumed K_I domain at the far-field boundary (red box) (**b**), taking the fully unloaded material (from $K_I = K_{max}$ to 0) as the reference configuration. (**c**) Traction distribution, separation distribution, and the cohesive zone law from PINN–J_R based on measurement data along ∂R_2^i and ∂R_2^{ii} in (**b**).

Figure 12: (**a**) Finite element analysis (FEA) with implementation of the PINN-predicted cohesive zone law along the crack front, with initial (residual) elastic strain field at $K_I = 0$. (**b**) FEA simulated elastic strain field at $K_I = K_{max}$. (**c,d**) Comparison of the S-XRD (symbols) versus FEA (lines) measurements of strain distributions along several vertical (**c**) and horizontal (**d**) cross-sections near the crack-tip, depicted by dashed-dot lines in (**b**).

Figure A1: Construction of auxiliary field $\hat{S}_2[\hat{\sigma}_{ij}, \hat{u}_j]$ with a traction free surface along $x_2 = 0$ but with non-zero displacements (**c**) by superposing the linear elastic solutions of two sinusoidal, periodic traction fields on lower (**a**) and upper half-spaces (**b**).

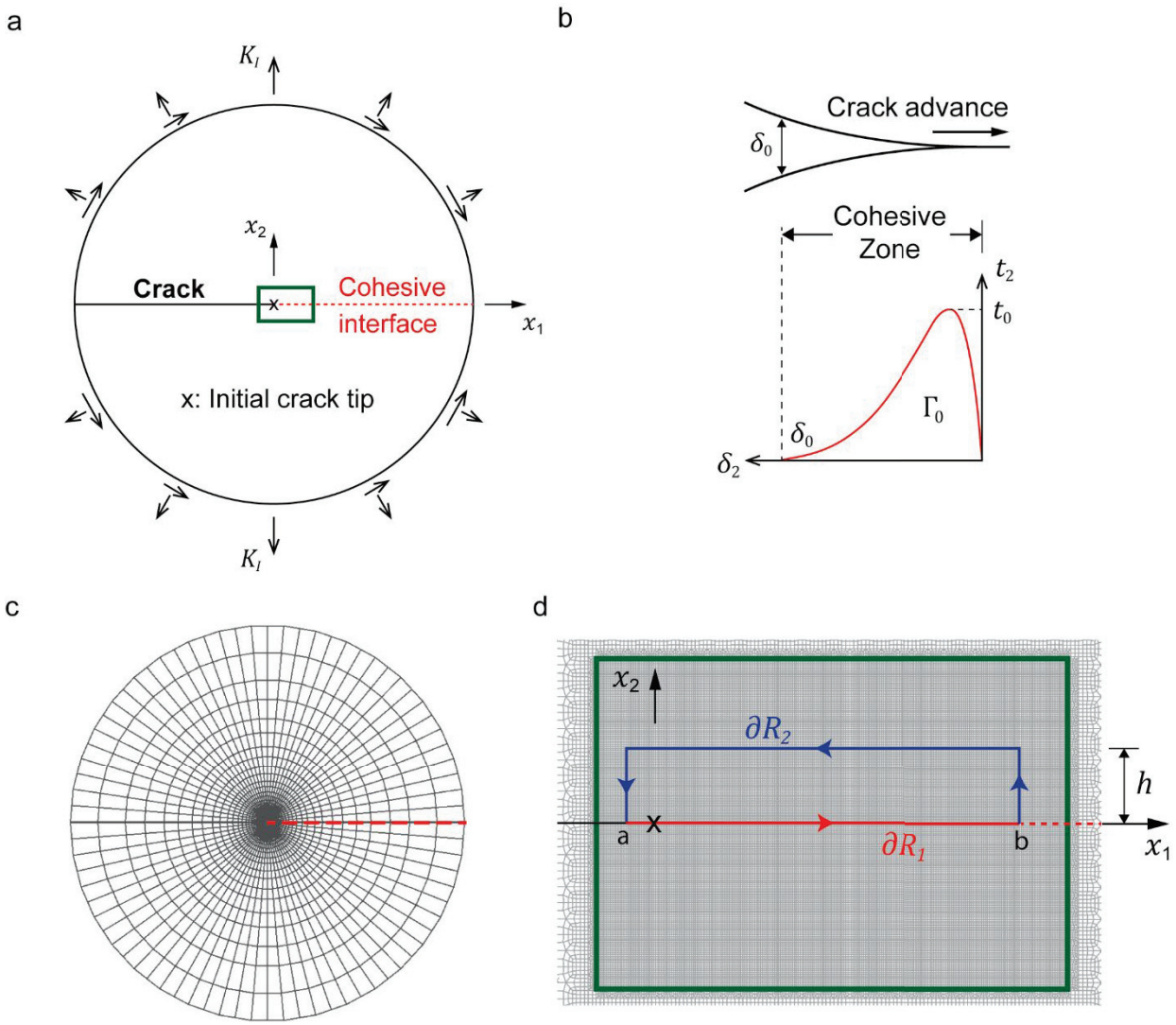

Figure 1: (**a**) Schematic of the small-scale yielding model with a centerline crack, subjected to remote mode I (K_I) loading, with a cohesive interface (dashed red line) in front of the crack tip located at $x_1 = x_2 = 0$. (**b**) Schematic of a cohesive zone, and a prescribed normal traction (t_2)-separation (δ_2) relationship. (**c**) Finite element mesh of the small-scale yielding model. (**d**) Close-up view of the highly-refined finite element mesh (green box) of uniformly sized $D \times D$ elements surrounding the initial crack tip (symbol 'x').

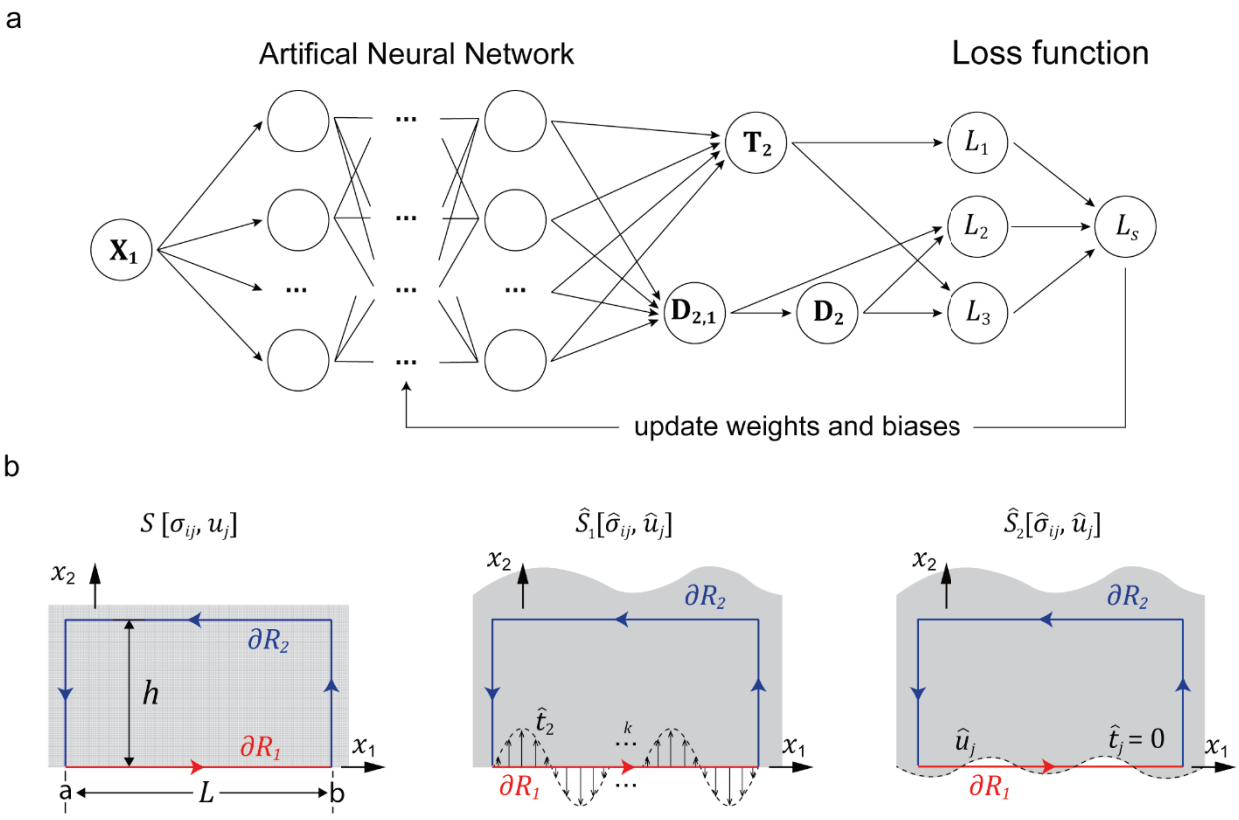

Figure 2: (**a**) Physics-Informed Neural Network (PINN) architecture for the reconstruction of the traction ($\mathbf{T_2}$) and separation distributions ($\mathbf{D_2}$) along the cohesive zone ($\mathbf{X_1}$) from far-field measurement data, subjected to physical and mechanistic constraints enforced by a loss function. (**b**) Schematic depicting the real field (S) and two classes of auxiliary fields ($\hat{S}_1, \hat{S}_2$) of the Maxwell-Betti's reciprocal theorem, which constitutes the primary constraint (L_3) linking measurement data along ∂R_2 (blue) to traction-separation predictions along ∂R_1 (red).

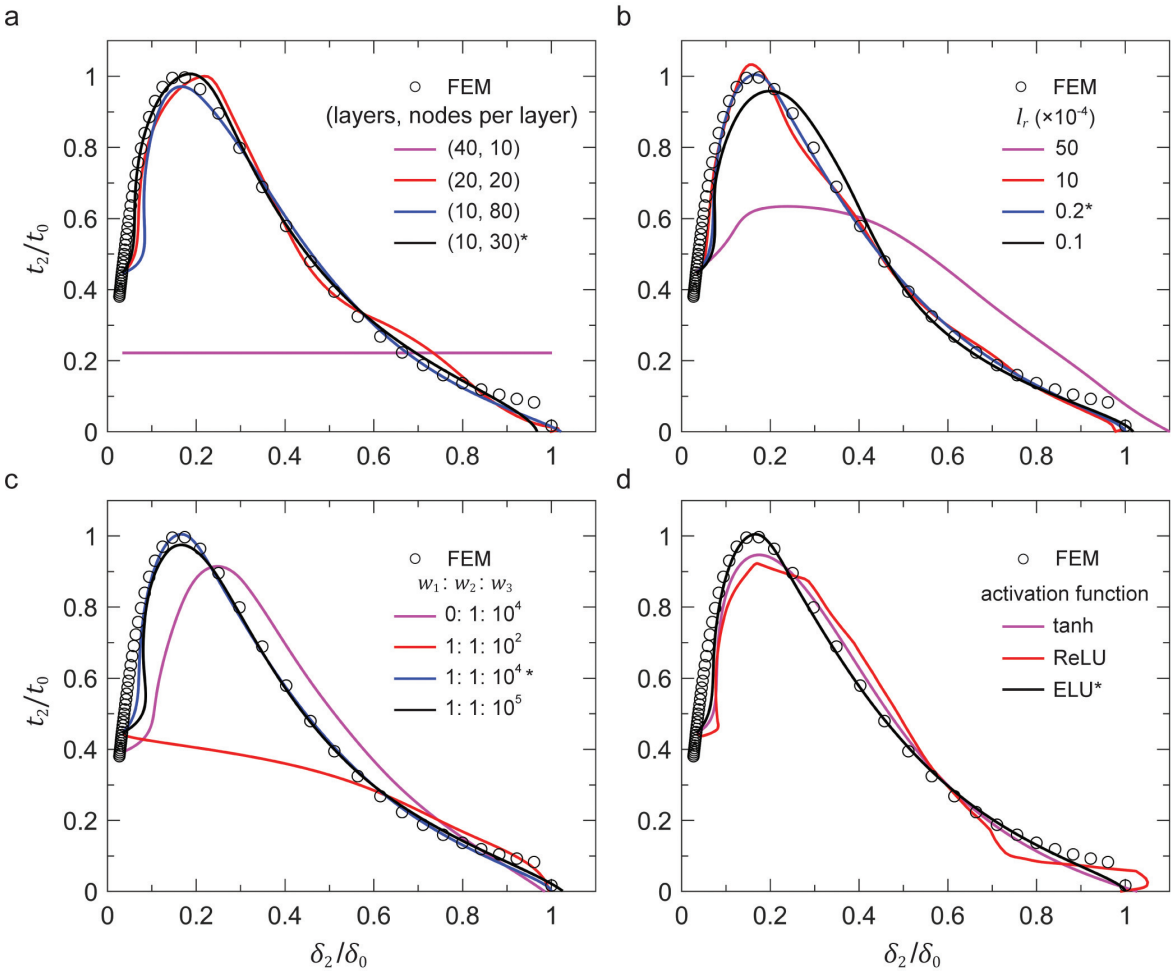

Figure 3: Hyperparameter studies on the network structure (**a**), learning rate (**b**), weights contribution of the loss function (**c**), and choice of activation function (**d**), depicting the PINN-predicted (lines) versus actual (symbols) exponential cohesive zone law; '*' supercript: locally optimal hyperparameters.

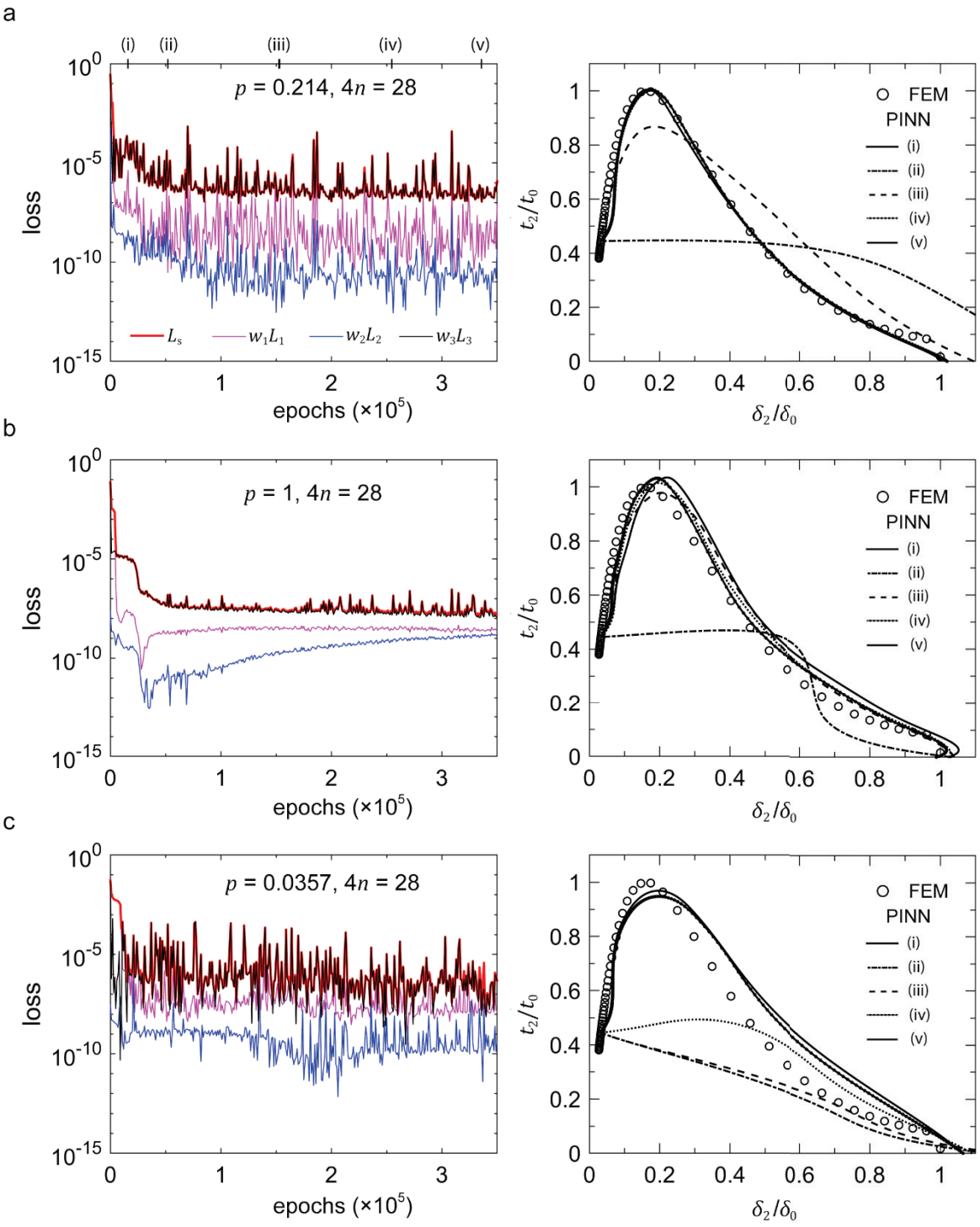

Figure 4: Weighted loss evolution (*left*) and convergence of the predicted exponential cohesive zone law with training epochs (lines, *right*) to ground truth data (symbols, *right*) for varying proportion (p) of terms enforced per epoch out of a fixed total number of constraints ($4n = 28$) in the reciprocal theorem.

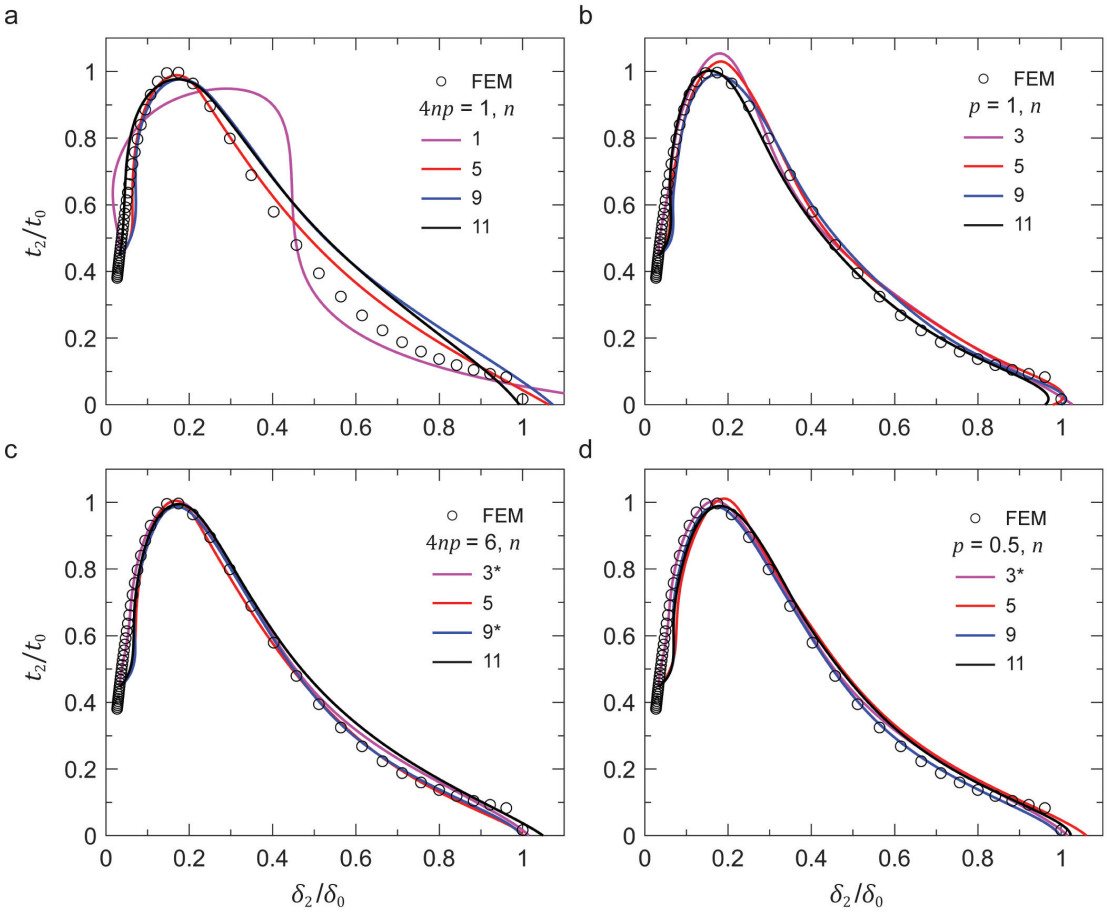

Figure 5: Predicted exponential cohesive zone law (lines) versus ground truth data (symbols) for different (n, p) combinations in the reciprocal theorem.

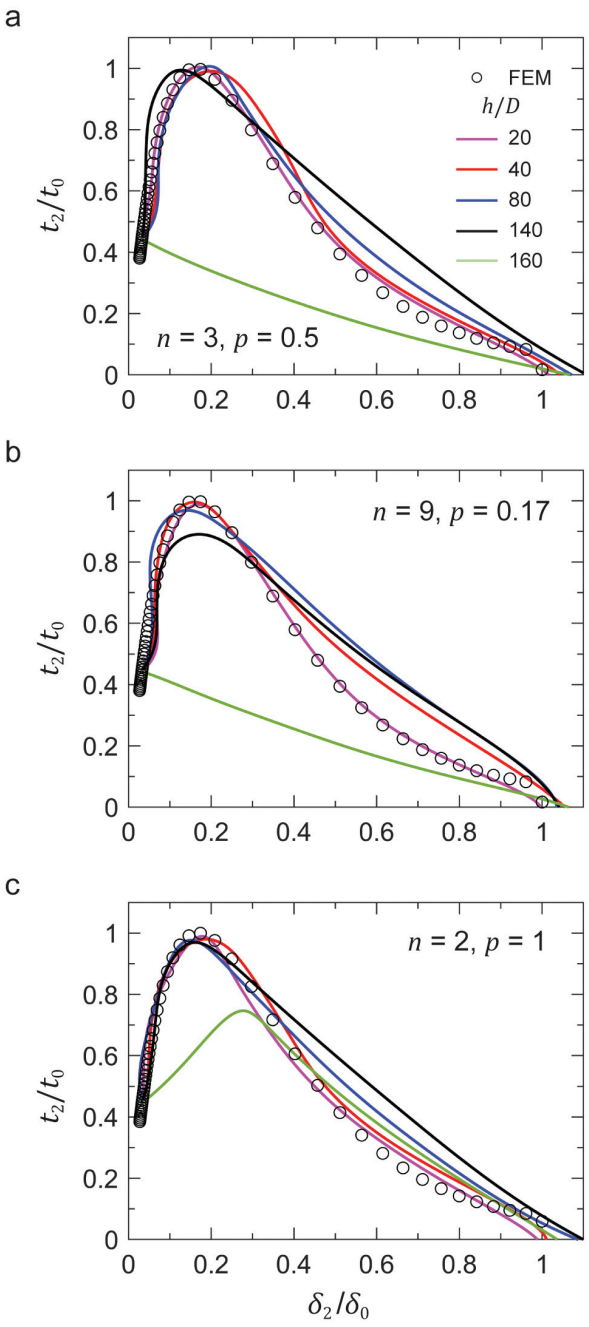

Figure 6: Domain size effects (h/D) on the predicted exponential cohesive zone law (lines) versus ground truth data (symbols) for different (n, p) combinations in the reciprocal theorem.

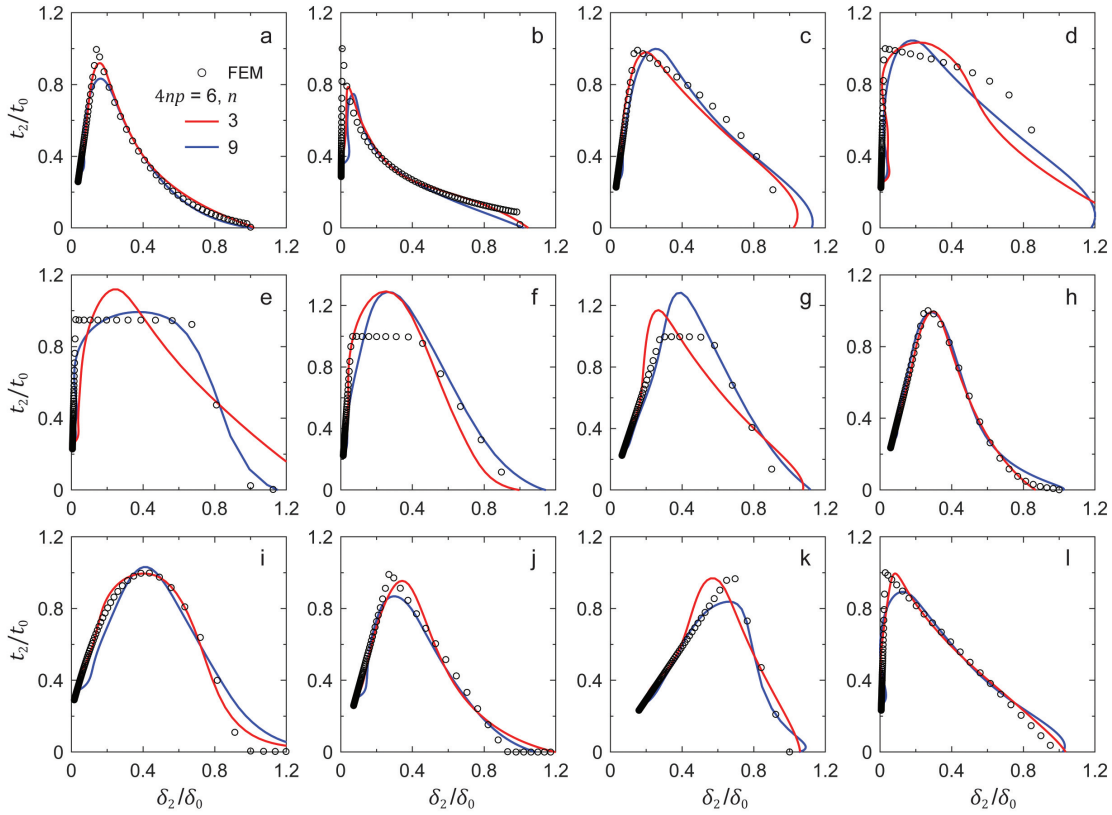

Figure 7: Predicted (lines) versus ground truth data (symbols) for different functional forms of the cohesive zone law.

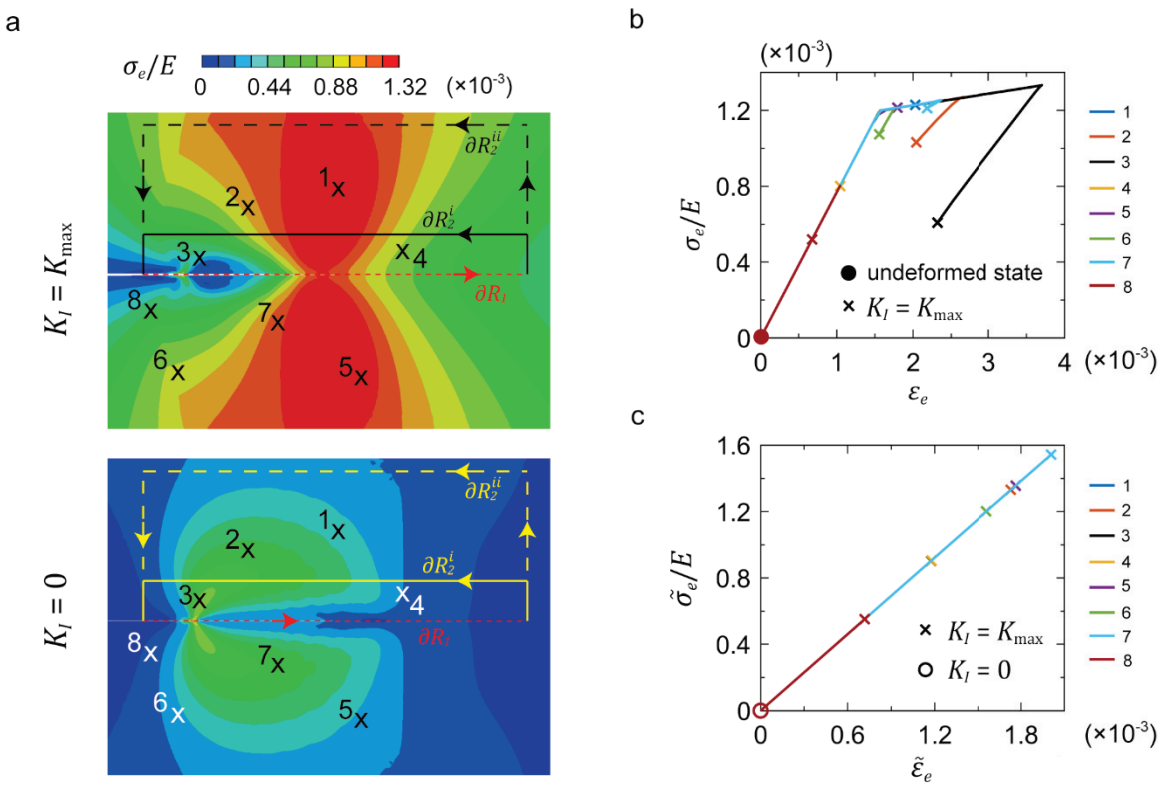

Figure 8: (**a**) Von Mises stress contours (σ_e/E) at the current loading $K_I = K_{max}$ and after unloading (from K_{max}) to $K_I = 0$. (**b**) Von Mises stress (σ_e/E) versus equivalent strain (ε_e) for material points 1-8 in (**a**) with the undeformed state ($\sigma_e = \varepsilon_e = 0$, circle symbol) as the reference configuration. (**c**) Von Mises stress ($\tilde{\sigma}_e/E$) versus equivalent strain ($\tilde{\varepsilon}_e$) for material points 1-8 in (**a**), taking the fully unloaded material ($K_I = 0$, circle symbol) as the reference configuration.

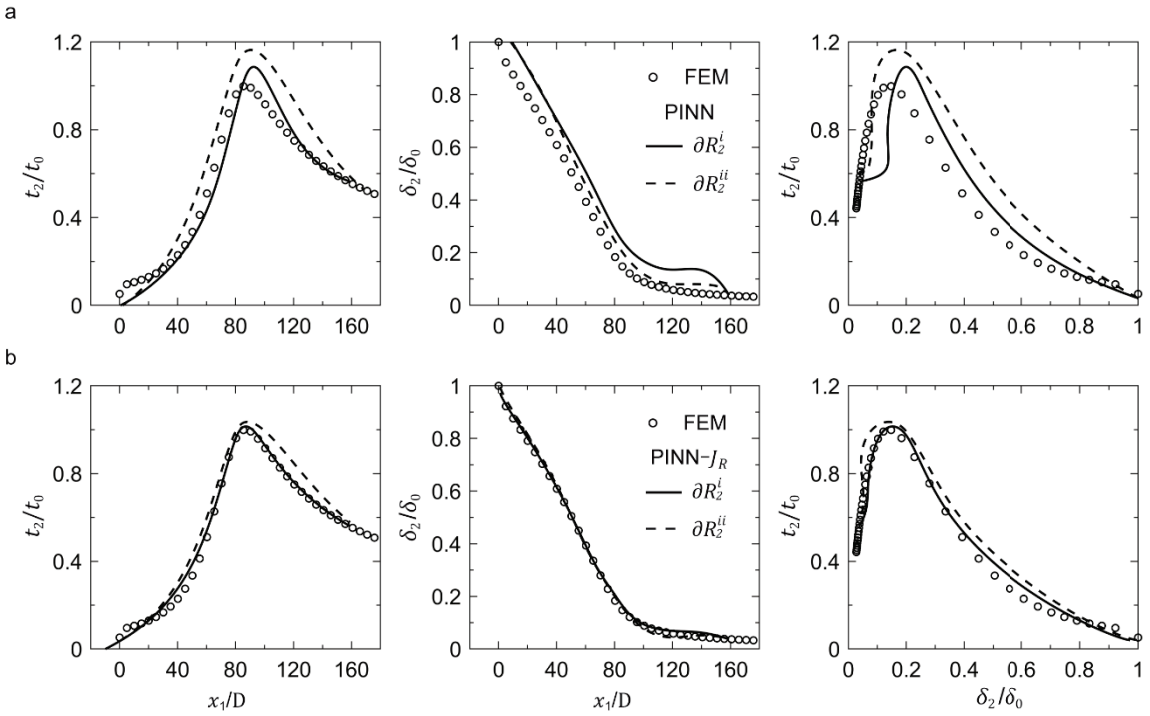

Figure 9: Traction distribution, separation distribution, and the cohesive zone law predicted by PINN (lines) from measurement data along two paths (∂R_2^i; ∂R_2^{ii}) versus actual ground truth data (circle symbols). (**a**) Original PINN formulation for linear-elastic materials. (**b**) Augmented PINN formulation (PINN–J_R) to account for plastically deforming background material.

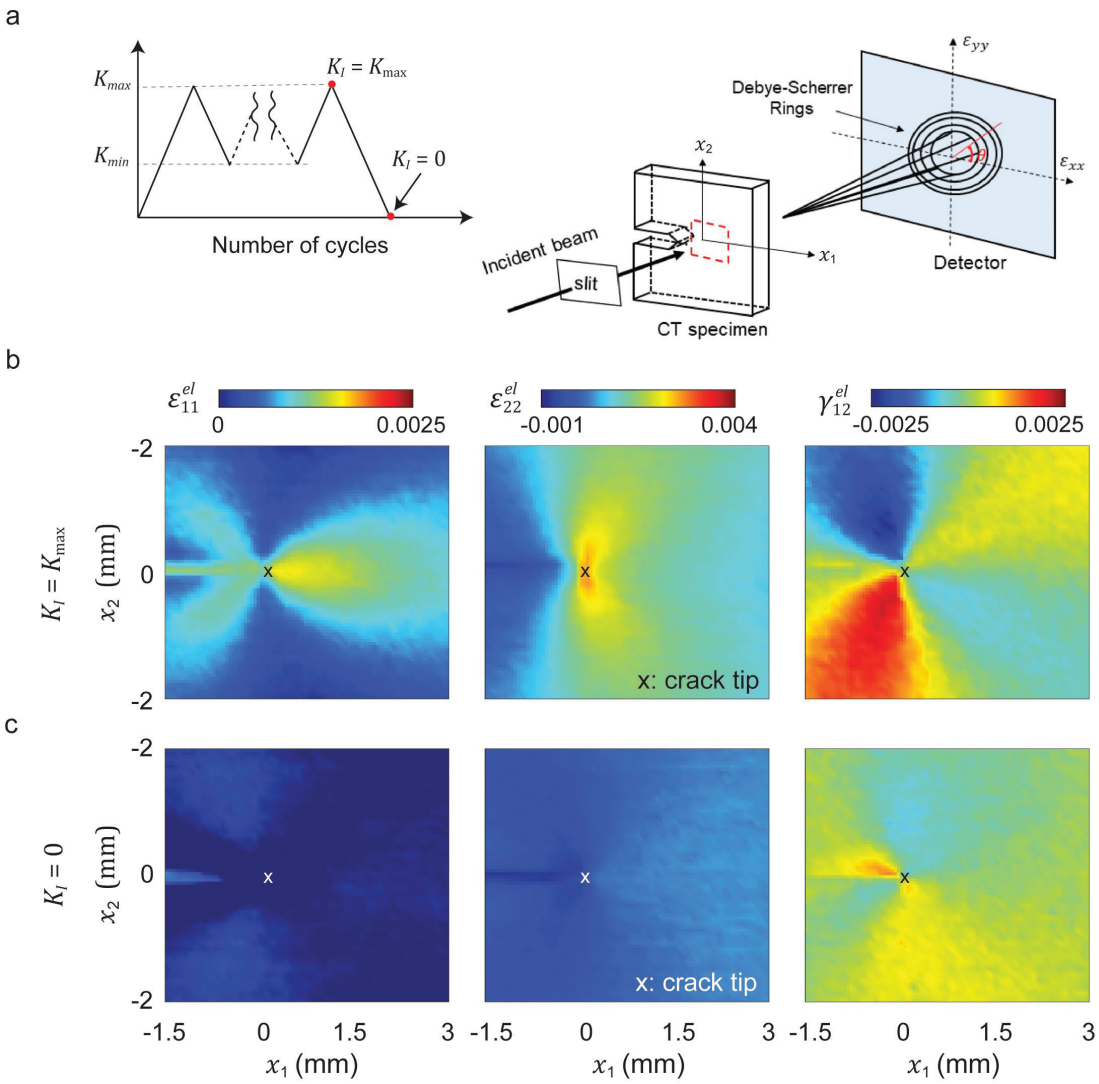

Figure 10: (**a**) Schematic of the diffraction setup for strain mapping measurement of a fatigue crack in a CT specimen using S-XRD, with mapping area in red dash square (Xie et. al., 2022). (**b,c**) Elastic strain measurement ($\varepsilon_{11}^{el}, \varepsilon_{22}^{el}, \gamma_{12}^{el} = 2\varepsilon_{12}^{el}$) from S-XRD at the last fatigue cycle, where the crack is fully unloaded from $K_I = K_{max}$ (**b**) to $K_I = 0$ (**c**).

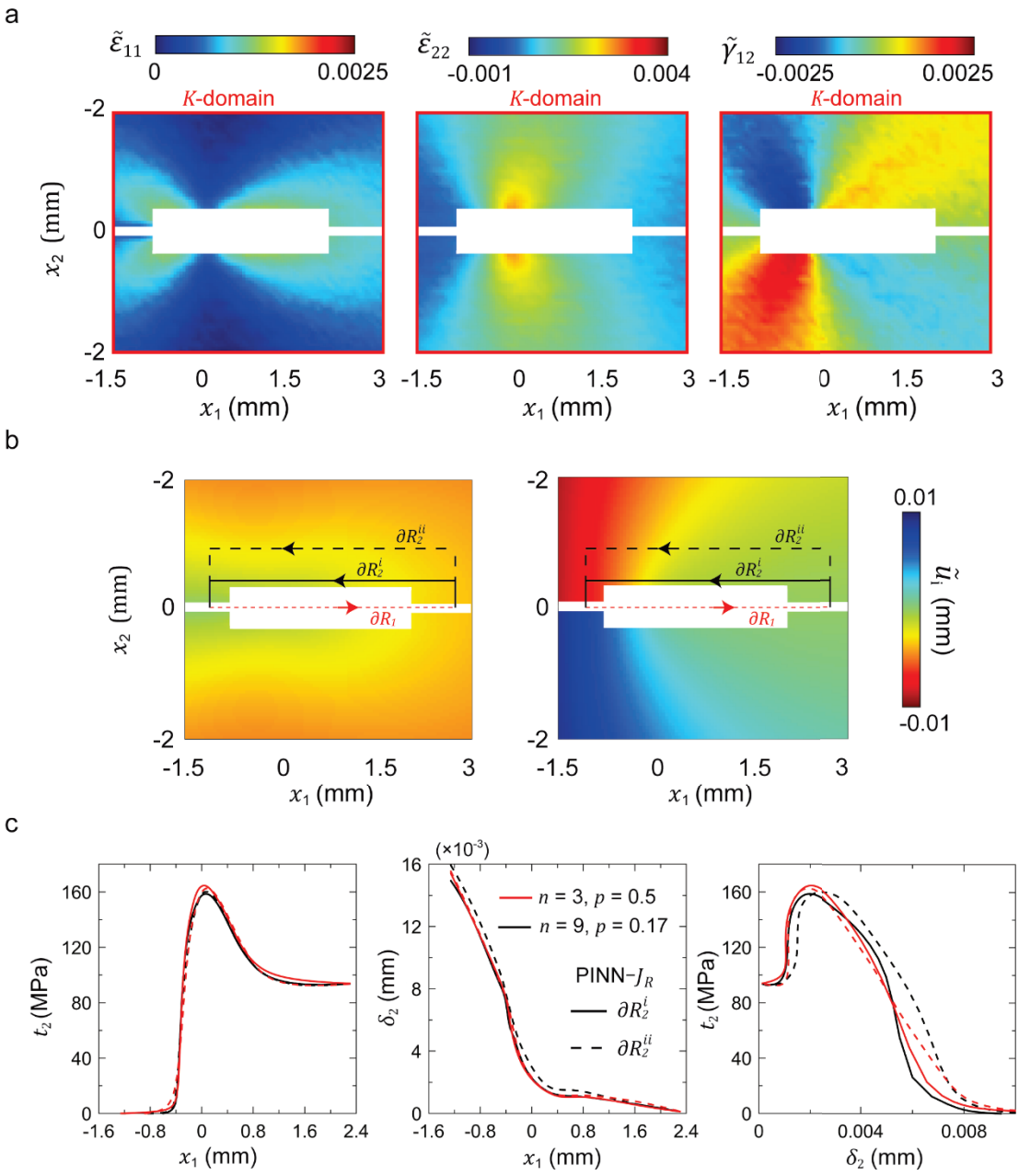

Figure 11: (**a**,**b**) Postprocessed S-XRD experiment elastic strain measurement ($\tilde{\varepsilon}_{11}, \tilde{\varepsilon}_{22}, \tilde{\gamma}_{12} = 2\tilde{\varepsilon}_{12}$) (**a**) and numerically reconstructed displacement field ($\tilde{u}_1, \tilde{u}_2$) with assumed K_I domain at the far-field boundary (red box) (**b**), taking the fully unloaded material (from $K_I = K_{max}$ to 0) as the reference configuration. (**c**) Traction distribution, separation distribution, and the cohesive zone law from PINN–J_R based on measurement data along ∂R_2^i and ∂R_2^{ii} in (**b**).

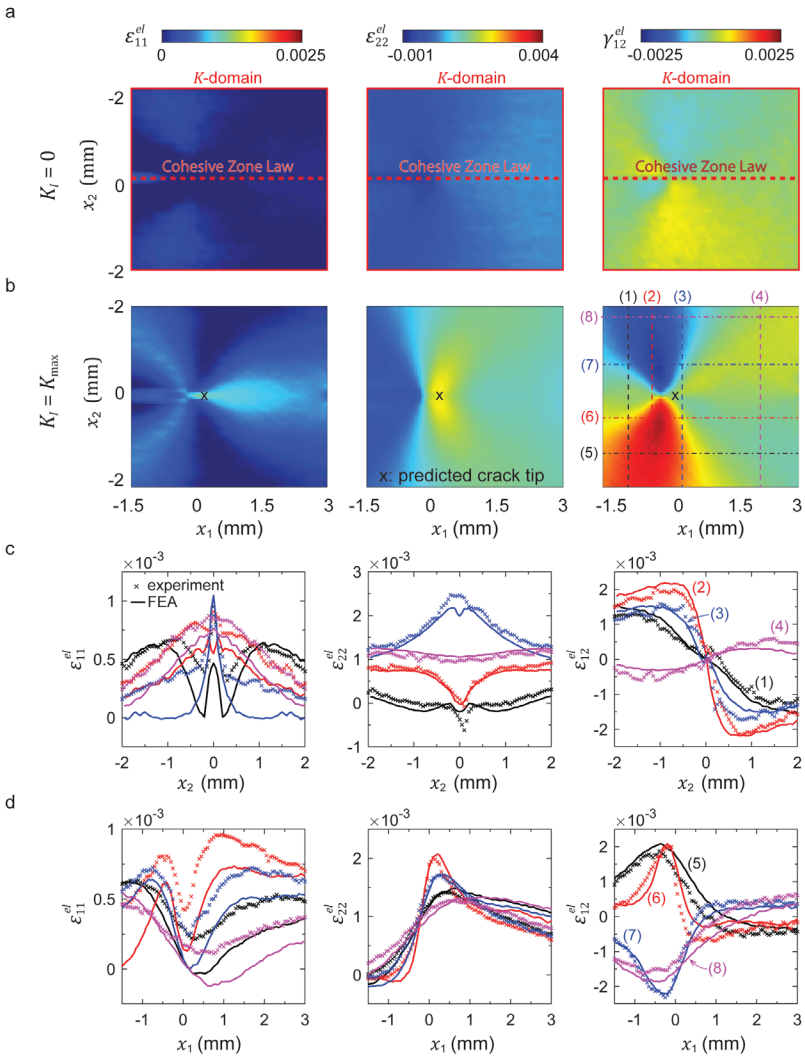

Figure 12: (**a**) Finite element analysis (FEA) with implementation of the PINN-predicted cohesive zone law along the crack front, with initial (residual) elastic strain field at $K_I = 0$. (**b**) FEA simulated elastic strain field at $K_I = K_{max}$. (**c,d**) Comparison of the S-XRD (symbols) versus FEA (lines) measurements of strain distributions along several vertical (**c**) and horizontal (**d**) cross-sections near the crack-tip, depicted by dashed-dot lines in (**b**).

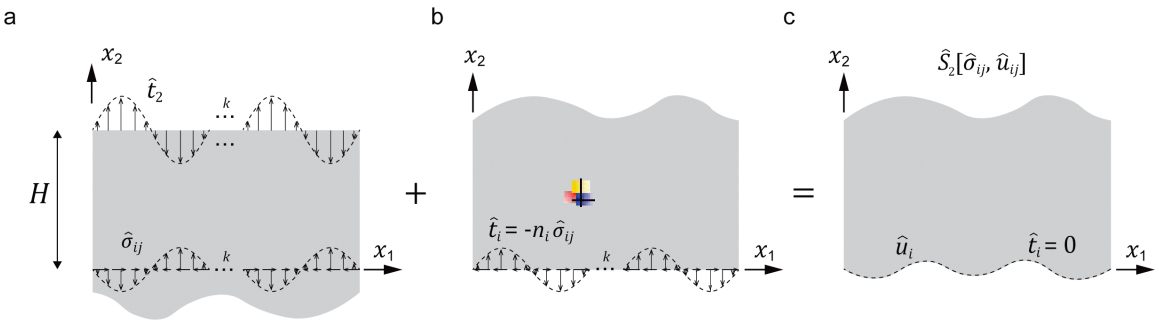

Figure A1: Construction of auxiliary field $\hat{S}_2[\hat{\sigma}_{ij}, \hat{u}_j]$ with a traction free surface along $x_2 = 0$ but with non-zero displacements (**c**) by superposing the linear elastic solutions of two sinusoidal, periodic traction fields on lower (**a**) and upper half-spaces (**b**).